2012-07-05

Modeling of Complex Pentahedron Solar Still Covers to Optimize Distillate

Jeremy D. LeFevre
Brigham Young University - Provo

BYU ScholarsArchive Citation

LeFevre, Jeremy D., "Modeling of Complex Pentahedron Solar Still Covers to Optimize Distillate" (2012). *Theses and Dissertations*. 3663.
https://scholarsarchive.byu.edu/etd/3663

Modeling of Complex Pentahedron Solar Still Covers to Optimize Distillate

Jeremy LeFevre

A thesis submitted to the faculty of
Brigham Young University
in partial fulfillment of the requirements for the degree of

Master of Science

W. Jerry Bowman, Chair
Matthew R. Jones
Christopher A. Mattson

Department of Mechanical Engineering

Brigham Young University

August 2012

ABSTRACT

Modeling of Complex Pentahedron Solar Still Covers to Optimize Distillate

Jeremy LeFevre
Department of Mechanical Engineering, BYU
Master of Science

This work shows the results of modeling and optimizing pentahedron-shaped covers for application on a passive solar still. While modeling under the assumption of clear weather in Provo, Utah, United States of America, it was found that two main geometries resulted:

1. A single slope still with fully vertical back and sidewalls and a south face tilted at 37.1°, absorbing a total of 8.98 megajoules of direct solar radiation.
2. A half-pyramid shaped cover with vertical backwall, sidewalls tilted in at 60.6°, and a south face tilted in at 41.5°, absorbing 9.34 megajoules of direct solar radiation.

With improved covers, solar radiation absorbed by the basin can be maximized. Maximum radiation absorbed will generally indicate maximum still output.

In addition, the internal convection of a passive solar still was modeled in order to compare with existing correlations to find the best convection correlation. The convection was modeled using Fluent 12 (CFD software package) and simulations were run for various geometries and temperatures. It was found that Shruti's correlation agreed the best with the CFD results. However, another possible correlation is suggested here which accommodates a higher range of Grashof numbers. For a correlation of the form $Nu = C \cdot Ra^n$, it was found that C = 1.02, 0.56, and 0.66, and n = 0.19, 0.24, and 0.24 for cover tilt angles of 15°, 30°, and 45° respectively. Also, Grashof number ranges are $4.0 \times 10^3 < Gr < 1.9 \times 10^7$, $4.0 \times 10^4 < Gr < 1.9 \times 10^8$, and $2.1 \times 10^5 < Gr < 1.0 \times 10^9$ respectively.

Keywords: Jeremy LeFevre, solar, still, distillation, desalination, water purification, thermal

ACKNOWLEDGEMENTS

Several of the faculty members here at BYU have made contributions to this work or directly to me. It would be an oversight to not briefly acknowledge their help and contributions.

First, thanks to Dr. Bowman for paying my tuition every semester and making sure I had TA work throughout the year. Also, thanks for lending me your reference materials on a regular basis and directing the research to be able to accomplish something in the allotted time.

Also, thanks to Dr. Jones and Dr. Mattson for being on my committee and being patient with me as my research slowly came along. A special thanks to Dr. Jones for all the help with the heat transfer courses (especially radiative heat transfer, which was vital to this work).

Thanks to Dr. Maynes for lending me research licenses and somehow getting me through advanced fluids and convective heat transfer.

Thanks to Skyler Chamberlain and Darrel Zeltner for working with me in various courses and always making time to visit with me every time I stopped by their offices.

TABLE OF CONTENTS

LIST OF TABLES

LIST OF FIGURES

NOMENCLATURE

Symbol	**Description**
$\forall$	Volume Enclosed by Cover (m^3)
$\forall_{basin}$	Volume of Basin (Water) (m^3)
$\forall_{cover}$	Volume of Cover Material (m^3)
A	Absorptive coefficient (unitless)
A_b	Basin Area (m^2)
A_c	Cover Area (m^2)
$A_{p,basin}$, A_i'	Projected area to basin of i^th cover surface (m^2)
C	Nusselt Correlation Constant Coefficient
c_p	Specific Heat at Atmospheric Pressure (J/kg K)
$c_{p,basin}$	Specific Heat of Basin (Water) (J/kg K)
$c_{p,cover}$	Specific Heat of Cover Material (J/kg K)
D_{AB}	Mass Diffusivity of Water into Air (m^2/s)
$\left(\frac{dE}{dt}\right)_{basin}$	Basin Energy Differentiated by Time (W)
$\left(\frac{dE}{dt}\right)_{cover}$	Cover Energy Differentiated by Time (W)
g	Acceleration Due to Gravity (9.81 m/s^2)
Gr	Grashof Number (unitless)

h	Internal Convective Heat Transfer Coefficient (W/m^2 K)
h_m	Mass Transfer Coefficient (m/s)
h_{ex}	External Convective Heat Transfer Coefficient (W/m^2 K)
H	Cover Height (m)
h_m	Convective Mass Transfer Coefficient (m/s)
I_N	Surface irradiation (W/m^2)
I_{ON}	Extraterrestrial irradiation (W/m^2)
k	Thermal Conductivity of the Fluid (W/m K)
K_1	Beam scattering perturbation factor (unitless)
K_2	Background diffuse irradiation (W/m^2)
L	Basin Length (m)
L_C	Characteristic Length
Le	Lewis Number (unitless)
m	Air mass (unitless)
n	Nusselt Correlation Exponent Coefficient
$\hat{n}_{sun}$	Unit Vector in Sun’s Direction (unitless)
$\hat{n}_{surface,i}$	Unit Vector Normal to ith Cover Surface (unitless)
Nu	Nusselt Number (unitless)
P	Operating Pressure of Still (Pa)
Pr	Prandtl Number (unitless)

q	Total Convective Heat Transfer (Watts)
$q_{convection,in}$	Internal Convective Heat Transfer (Watts)
$q_{convection,ex}$	External Convective Heat Transfer (Watts)
$q_{evaporation}$	Heat Transfer by Mass Transfer (Watts)
q_{losses}	Heat Losses from Basin (Watts)
$q_{solar,total}$, $q_{solar,absorbed}$	Total solar power absorbed (Watts)
$Q_{solar,total}$	Total solar energy absorbed (MJ)
q_w''	Wall Heat Flux (W/m^2)
R	Reflective coefficient (unitless)
Ra	Rayleigh Number (unitless)
R_{air}	Universal Gas Constant of Humid Air (J/kg K)
S	Sutherland Temperature (K)
T	Transmissive coefficient (unitless)
t	Cover thickness (m)
T_∞	Ambient/Surroundings Temperature (K)
T_{basin}	Basin Temperature (K)
T_{cover}	Cover Temperature (K)
T_{film}	Film Temperature (K)
T_H	Basin Temperature (K)
T_L	Cover Temperature (K)
T_R	Linke turbidity factor (unitless)
T_{ref}	Reference Temperature (K)

U_{losses}	Basin Loss Heat Transfer Coefficient (W/m^2)
W	Basin Width (m)
x_1	X coordinate of projected point 1 (m)
x_2	X coordinate of projected point 2 (m)
y_1	Y coordinate of projected point 1 (m)
y_2	Y coordinate of projected point 2 (m)
α	Additional intensity depletion factor (unitless)
α	Absorptivity (unitless)
α_{basin}	Basin Absorptivity (unitless)
γ	Azimuth angle (degrees or radians)
∂	Declination angle (degrees or radians)
ΔT	Temperature Difference (K)
ε	Rayleigh optical thickness of atmosphere (unitless)
θ_{basin}	Basin Tilt Angle (degrees)
θ, θ_{cover}	Cover Tilt Angle (degrees)
$\theta, \theta_i, \theta_{cover}$	Incident angle (degrees or radians)
θ_z	Zenith angle (degrees or radians)
κ	Attenuation coefficient (m^{-1})
μ	Viscosity (Pa s)
μ_{ref}	Reference Viscosity (at T_{ref}) (Pa s)
ρ	Reflectivity (unitless)

ρ	Density (kg/m^3)
ρ_{basin}	Density of Basin (Water) (kg/m^3)
$\rho_{basin,sat}$	Water Saturation Density at Basin Termperature (kg/m^3)
ρ_{cover}	Density of Cover Material(kg/m^3)
$\rho_{cover,sat}$	Water Saturation Density at Cover Termperature (kg/m^3)
τ	Transmissivity (unitless)
φ	Latitude (degrees)
φ_{cover}	Cover Tilt Angle (degrees)
χ	Refracted angle (degrees or radians)
ω	Hour angle (degrees or radians)

1 INTRODUCTION

Providing access to clean water is rated as the third greatest challenge of engineering according to engineeringchallenges.org [1]. The National Academy of Engineers estimates 1 in 6 people in the world do not have adequate water, and as a result, water shortages are responsible for more deaths globally than war.

The UN's 2006 Human Development Report [2] estimates that around 2 million children die each year due to lack of sanitary drinking water. They also claim that the problem itself is perpetuated due to its negative influence on the economies of developing countries.

1.1 Desalination

Desalination is a popular solution to the world's water problems because 97% of the earth's water is too salty to drink [3]. The earth naturally desalinates water by evaporating ocean water, leaving the salt in the oceans. When the humidified air cools, the water precipitates and falls as rain. This natural process has inspired the engineering process known as solar distillation.

1.2 Solar Distillation

Figure 1-1 shows the basic setup of a solar still and also gives some basic terminology. A typical passive solar still is very simple, composed of three main parts: a basin, a cover, and a trough that leads to the distillate reservoir. The brackish water is evaporated by solar radiation and the water vapor condenses on the cover. After condensing into large enough drops, the water collects into the distillate troughs. The setup shown has an inclined basin, but most simple stills have a basin tilt angle of zero for simplified manufacturing. Tiwari [4] cited multiple sources showing that the dominant factor in solar still production is insolation. Anything that can increase the insolation on the basin will improve the performance of the still.

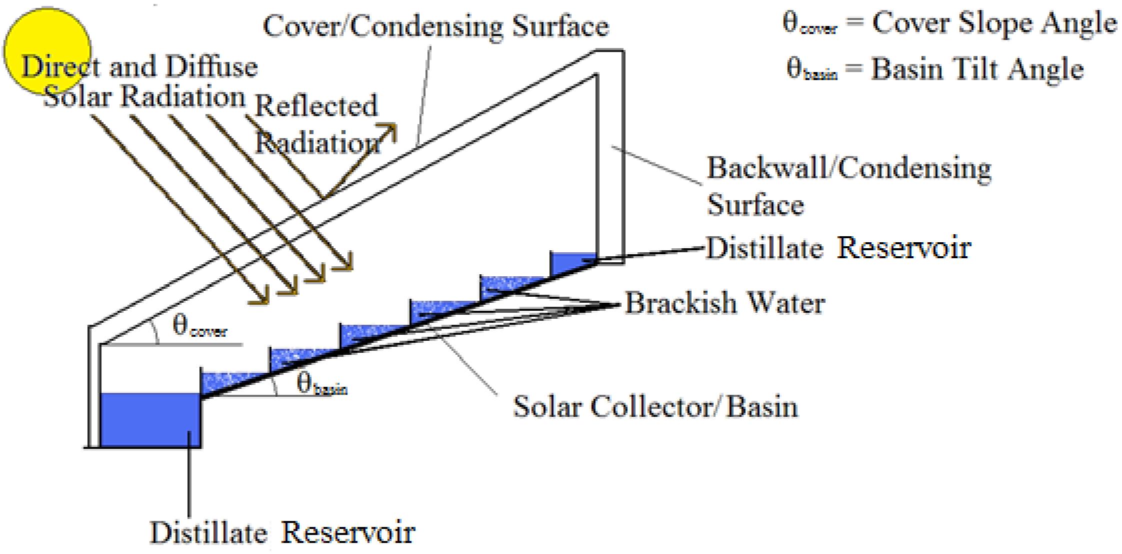

Figure 1-1: Basin Solar Still Diagram and Terminology

1.3 Basic Solar Still Model

Analytical models of solar stills can be derived from a simple energy balance. When developing any thermal model, there are usually several heat transfer processes to account for. It is important to model the highest magnitude processes first. In the case of the solar still, a few main processes dominate the model: solar input, internal convection, internal mass transfer (evaporation), and basin heat losses. Figure 1-2 shows a diagram illustrating these heat transfer processes.

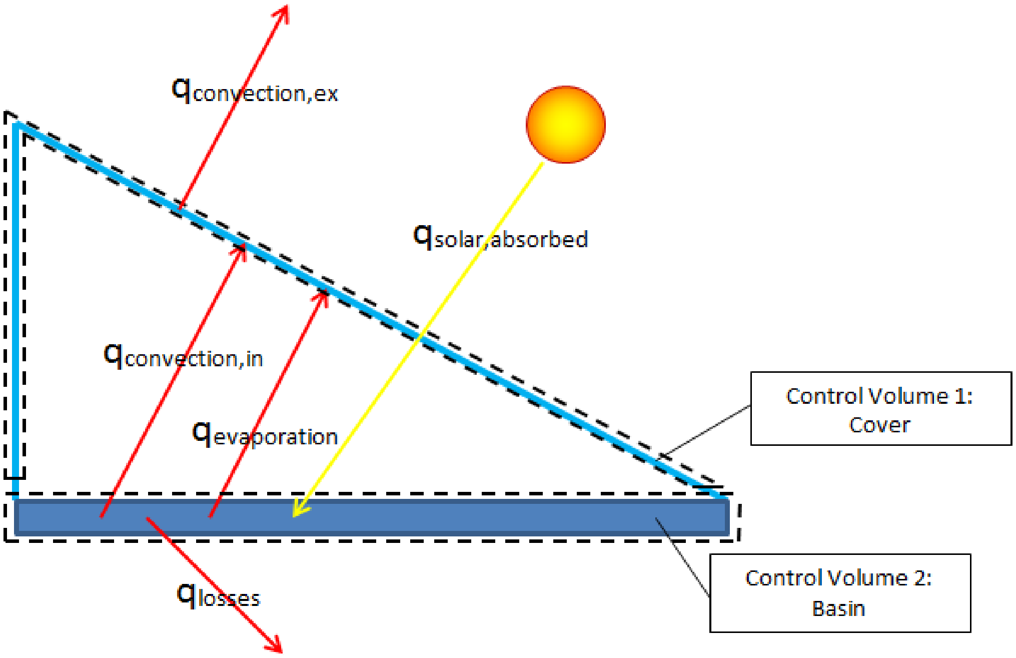

Figure 1-2: Diagram of Energy Processes

The cover and basin can be treated as control volumes, and energy balances can be performed on each. The cover yields the equation[1]

$$\left(\frac{dE}{dt}\right)_{cover} = q_{convection,in} + q_{evaporation} - q_{convection,ex}, \tag{1-1}$$

and the basin yields the equation

$$\left(\frac{dE}{dt}\right)_{basin} = q_{solar,absorbed} - q_{convection,in} - q_{evaporation} - q_{losses}. \tag{1-2}$$

Each term can be modeled individually as shown below.

$$q_{convection,in} = hA_b(T_{basin} - T_{cover}) \tag{1-3}$$

$$q_{evaporation} = h_m A_b(\rho_{basin,sat} - \rho_{cover,sat}) \tag{1-4}$$

$$q_{convection,ex} = h_{ex} A_c(T_{cover} - T_\infty) \tag{1-5}$$

$$q_{solar,absorbed} = \alpha_{basin} I_N \cos\theta_z \sum_{i=1}^{4} T_i A_i' \tag{1-6}$$

---

[1] All symbols can be found in the NOMENCLATURE.

$$\boldsymbol{q_{losses} = U_{losses} A_b (T_{basin} - T_\infty)} \tag{1-7}$$

$$\left(\frac{dE}{dt}\right)_{cover} = \left(\rho c_p \forall\right)_{cover} \frac{dT_{cover}}{dt} \tag{1-8}$$

$$\left(\frac{dE}{dt}\right)_{basin} = \left(\rho c_p \forall\right)_{basin} \frac{dT_{basin}}{dt} \tag{1-9}$$

The coefficients h, h_m, h_{ex}, and U_{losses} are typically modeled using correlations found from experimental data or numerical modeling. In order to have an accurate thermal model, each of the energy balance terms must be modeled accurately. Specifically, they must capture the major effects of changing the cover geometry in order to be able to compare designs. In order to perform an optimization of the still, a model is required that can account for changes in the cover geometry. Modeling $q_{convection,in}$ and $q_{solar,absorbed}$ become particularly important when determining still performance, and are the subject of this research. Specifically, finding the projected basin area (A_i') and the convection coefficient from a Nusselt correlation ($Nu = f(Gr,Pr)$).

1.4 Research

The analytical model may be used to optimize the geometry and increase total radiation to a solar still basin. Popular designs of passive solar stills include single slope stills, roof type stills, and cone shaped stills (see Figure 1-3). Beginning in the early 1970's, researchers have looked into optimizing the cover slope angle for single slope stills and roof angle for different times of the day or year. Single slope and roof type solar stills lose some solar radiation due to reflection when the sun is not perfectly normal to the cover surface. A different geometry might improve the production of solar stills by transmitting more radiation. In this work, an analytical model was created to evaluate the benefits of a complex pentahedron shaped cover versus a single slope or roof shaped covers (see Figure 1-4).

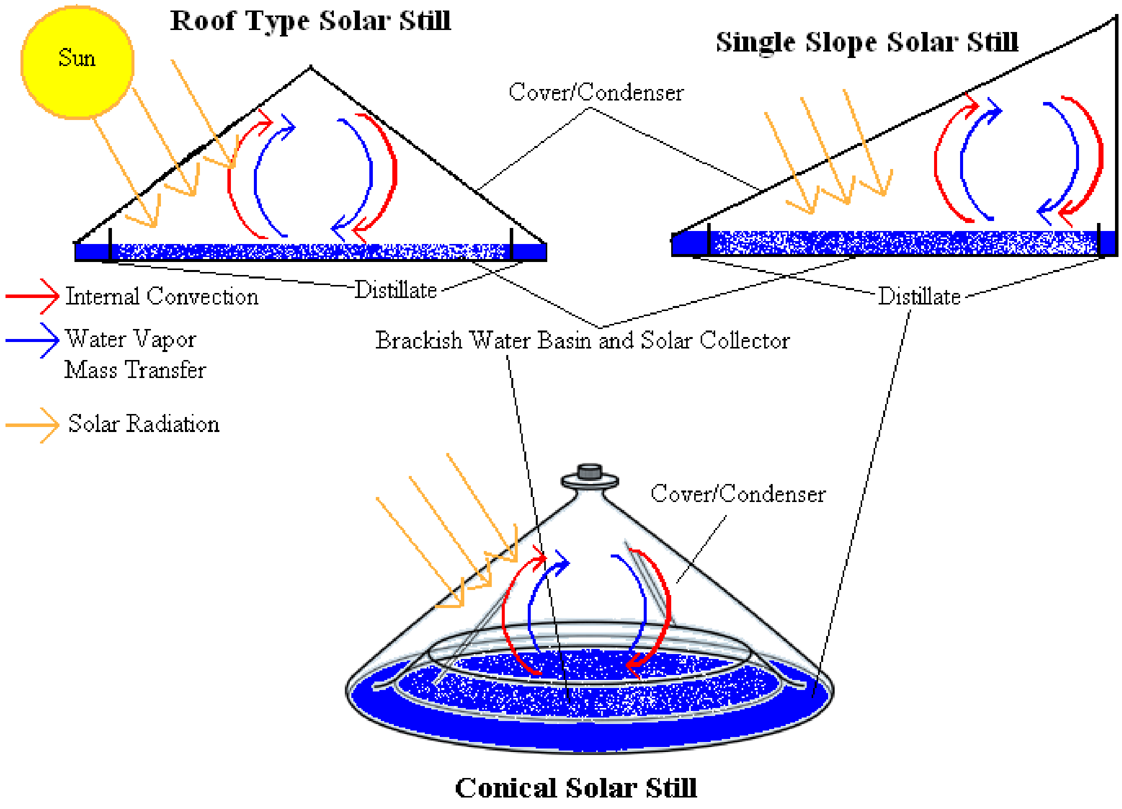

Figure 1-3: Popular Slope Cover Designs (conical still image modified from Watercone [11])

Much work has been done to optimize the angle of solar still covers and solar collectors in general. It is generally agreed that the ideal slope for a given collector or cover is the latitude of the location (for annual energy collected or annual yield). In 2004, Singh [5] experimentally verified that the optimum angle for both the collector and the cover is the latitude of the location. Ulgen [6] calculated the optimum solar collector angle for Izmir, Turkey (38 degrees latitude) at 30.3 degrees. For West/East facing sloped solar stills, it was found by Tiwari [7] that the optimum cover angle was about 55 degrees (probably due to internal convective effects). Effects such as weather patterns, pollution, convection and condensation loss can also change the ideal angles mentioned above (for example the optimum for Izmir, Turkey, deviates about 8 degrees from the latitude).

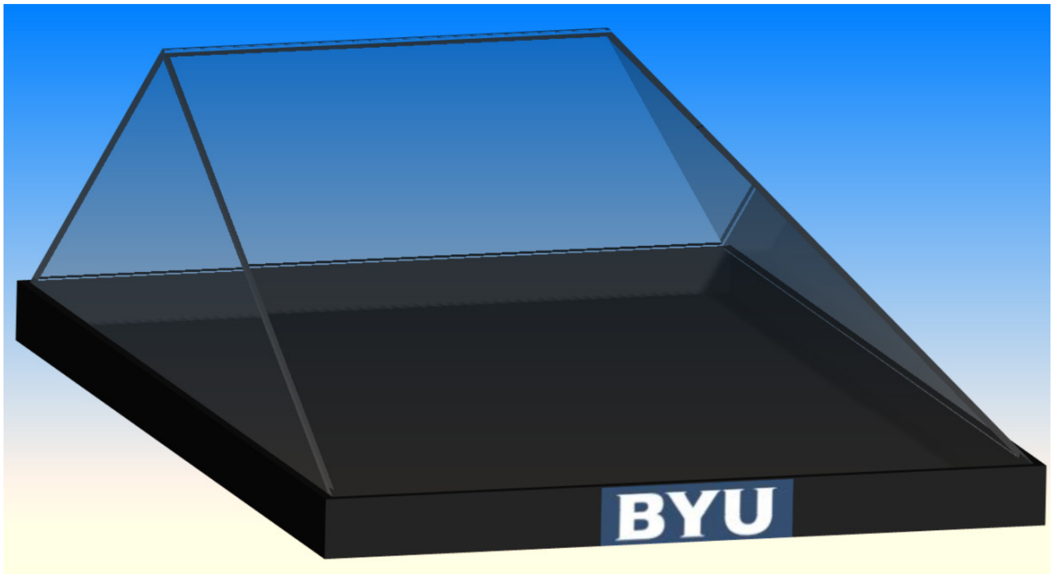

Figure 1-4: Simple Concept Rendering of a Pentahedron Still

Pentahedrons are not totally new designs, and Sayigh [8,9] has done some experiments comparing dome covers to pyramid shaped covers. In his research, he found that a pyramid shaped cover produced more distillate in an active still setup (warm water was pumped through the basin trays). Fath [10] found from experimental data that pyramid type stills are less economical than single slope stills. However, annual production was comparable, suggesting that if the angles of the different faces were optimized to improve inlet of solar radiation, production might be increased.

Another item of interest in the solar distillation community is finding convection correlations to better predict still performance for a variety of conditions. A difficulty that arises when changing the cover geometry is the effect that it has on the internal convection. While many correlations exist, most fail to account directly for the change in relationship between the Grashof and Nusselt number as the cover shape changes.

1.5 Objectives

The goals for this research were:

1. Modeling three types of solar still covers, a single slope, a roof type, and a complex pentahedron.
2. Compare the radiation absorbed by the basin for any given day of the year for each still based on irradiance data and solar altitude and azimuth angles.
3. Find geometric parameters that optimize each cover type for maximum solar radiation capture.
4. Perform an analysis that predicts the convection coefficients for different cover geometries to find a relationship between Nusselt and Grashof for those geometries.

2 MAXIMIZATION OF ABSORBED RADIATION FOR A PENTAHEDRON COVER GEOMETRY FOR APPLICATION IN A PASSIVE SOLAR STILL[2]

2.1 Introduction and Review of Literature

Solar still cover geometry is always a topic of interest when it comes to designing the best possible solar still. Several different geometries have been explored but no real consensus to the best geometry has ever been decided upon (perhaps because several parameters can favor certain geometries under certain conditions). Ismail built and tested a hemispherical solar still and was able to achieve outputs from 2.8 to 5.7 L/m^2 per day under summer climatic conditions in Dhahran [12]. Minasian constructed and tested a conical solar still with a wick parallel to the cover, instead of a basin. It was found to produce from 2 to 4 L/m^2 per day in Baghdad over the year [13]. Tiwari conducted a test of fiber reinforced covers which compared the performance of the single slope cover to the double slope cover (roof type) directly, and found that season was the main factor in determining which geometry to use. Findings indicated that the double slope produced 0.7 to 1.15 L/m^2 per day during winter and 2.48 to 2.85 L/m^2 per day during summer. The single slope produced 0.74 to 1.10 L/m^2 per day during winter and 2.21 to 2.40 L/m^2 per day during summer [14]. Finally, Fath has done a large amount of work on pyramid shaped covers, which were found to produce about the same amount of distillate per day as a single slope still (2.6 L/m^2, the annual average for Aswan, Egypt) [10]. This work looks at a direct comparison of three different cover geometries and optimizes each for conditions in Provo, Utah, United State of America.

---

[2] Chapter submitted for publishing in *Desalination*.

2.2 Statement of Intent

Three main cover geometries, discussed in this paper, have become the most widely used and studied for passive, basin type solar stills. These include single slope, roof type, and pyramid shaped covers. The main objective of this research was determining the geometry that would maximize solar radiation to the basin. The cover geometry that optimizes solar radiation to the basin would indicate the best candidate for application in a solar still. On the other hand, the candidate that can produce the highest amount of distillate per day per unit cost could be a good candidate as well. The three geometries studied are illustrated in Figures 2-1 to 2-3.

2.2.1 Geometries Currently Favored

Currently, the most commonly used solar still is the single slope configuration. It's a simple design and abundant research [15-17] has been done to evaluate its performance at various locations under various climatic conditions. For this configuration, the cover faces south (For this work, the still was assumed to be located in the northern hemisphere). One of the most famous solar stills (built by Charles Wilson near Las Salinas, Chile) appears to have been a single slope configuration [18]. Probably the next most popular cover type is the roof type (sometimes called double slope). In this configuration, the covers face east and west. Roof type covers typically have reduced performance at high latitudes or during the winter. Recently, there has been increasing interest in pyramid shaped stills [10, 19-20]. The faces of pyramid stills face all four directions (north, south, east, and west).

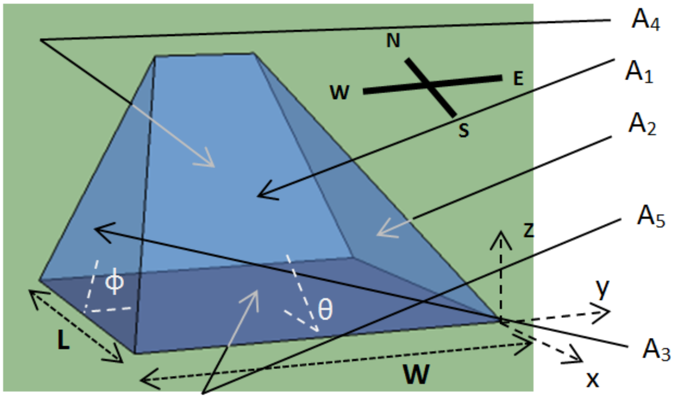

Figure 2-1: Single Slope Cover

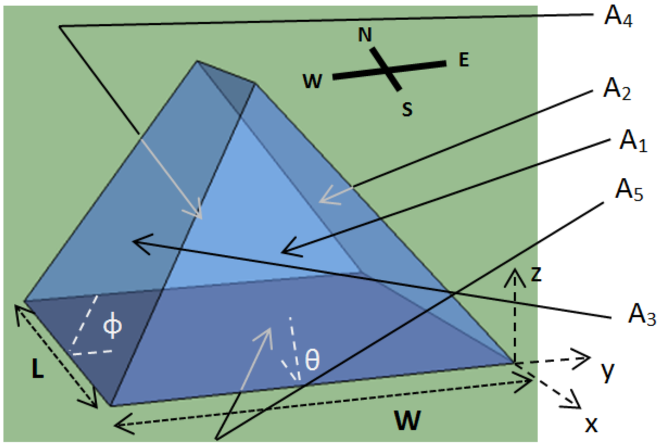

Figure 2-2: Double Slope or Roof Type Cover

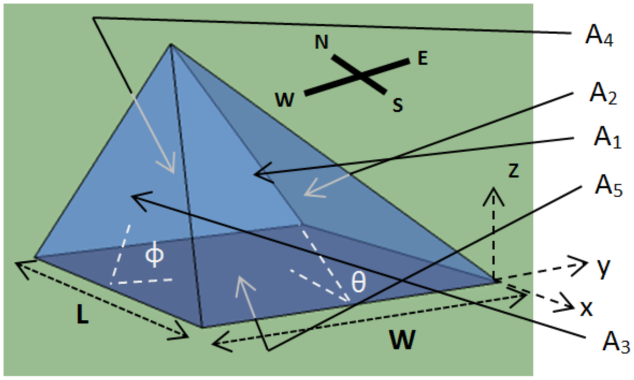

Figure 2-3: Half Pyramid Shaped Cover

2.2.2 Geometries Explored in the Current Study

The current study used variations on the three covers mentioned above. However, each geometry was allowed to vary within certain parameters. The following describes how they were allowed to vary.

Roof-type (double slope, east-west facing) solar stills studied in this work have two sides both inclined at an angle φ to the horizontal, and a front face that could be vertical (as a traditional double slope cover) or could be inclined at an angle θ so long as the sides remain trapezoidal. The back face is vertical (Figure 2-2).

The half-pyramid, Figure 2-3, is basically a pyramid shape cut in half, with the cut face oriented toward the north. The half-pyramid was chosen instead of a full pyramid because over the course of the year, very little or no direct radiation will enter the rear surface of the cover, so it is less beneficial to try to orient it favorably to the sun (especially during winter or at high latitudes).

A single slope still is basically shaped like a wedge. Typically a single slope still has an inclined front face with vertical sidewalls. The cover has been modified in this case to allow the sides to collapse inward such that their tilt angle is φ, as long as the front face remains trapezoidal (Figure 2-1).

2.2.3 Varying Orientation and Shape of the Cover

The cover's faces (sides and front) were tilted and altered to optimize the total solar radiation to the basin. All three geometries were optimized to find which configuration allowed for the most radiation to the basin.

2.3 Modeling Process

Modeling the radiation through the cover of a solar still required several calculations. Finding the radiation to the basin was broken down into three main steps: Modeling the direct solar radiation source, modeling projected basin areas, and modeling the properties of the cover material.

2.3.1 Solar Radiation Modeling

The first major step to finding the solar radiation to the basin was to accurately model the irradiation provided by the sun at the relevant time of day and day of year. For a solar still, this required a model of the solar irradiation over the entire course of the day. The general model used here was from Tiwari's text [4].

The irradiation and the direction of the sun depends on the time of year, as well as the time of day. First, the time of year was determined, then the position of the sun was determined over the course of the defined day. For the current study, the maximum annual average was desired, so the autumnal equinox was selected (which will yield the same optimum as the annual average).

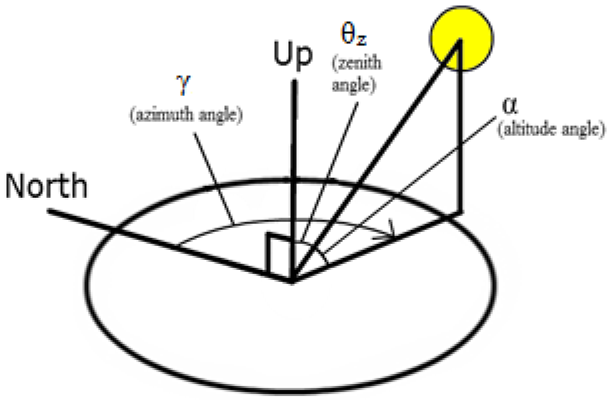

Figure 2-4: Azimuth, Zenith, and Altitude Angles Defined

With the day of the year fixed, the sun's position is defined by sweeping out two angles across the sky: the zenith angle and the azimuth angle (see Figure 2-4). Zenith angle (θ_z) is defined as the angle between the sun and the vertical direction. Azimuth angle (γ) is measured between the vector produced by projecting the direction of the sun to the horizontal (in other words, the NSEW direction of the sun) and a vector that points in the north direction along the horizontal. Equations for both have been developed based on the geographic location (φ, latitude), time of year (δ, declination angle), and time of day (ω, hour angle) [4].

$$\boldsymbol{\theta_z = cos^{-1}[cos\,\phi\ \ cos\,\delta\,cos\,\omega + sin\,\delta\,sin\,\phi]} \qquad \textbf{(2-1)}$$

$$\boldsymbol{\cos\gamma = \begin{cases} \frac{\sin\delta\cos\phi - \cos\omega\cos\delta\sin\phi}{\cos\alpha}, if\ \ \sin\omega < 0 \\ \frac{\cos\omega\cos\delta\sin\phi - \sin\delta\cos\phi}{\cos\alpha}, if\ \ \sin\omega > 0 \end{cases}} \qquad \textbf{(2-2)}$$

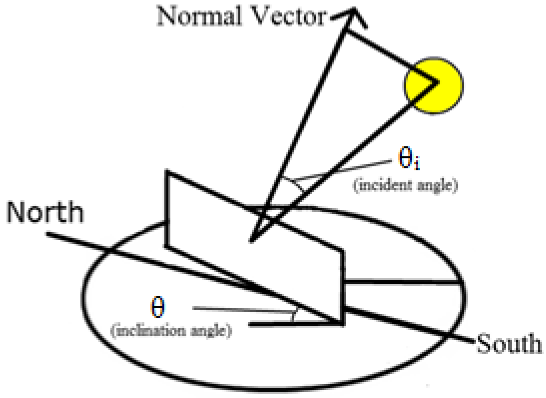

Figure 2-5: Radiation Model Geometry

The magnitude of solar irradiation depends on both the time of year, the time of day, and the current atmospheric conditions. Probably the most difficult variables to model are the current atmospheric conditions, as they are free to vary over the course of the day. In this study, atmospheric conditions were assumed to be clear and non-hazy (which lead to assuming parameters $T_R = 3.81$, $\alpha = 0.08$, $K_1 = 0.32$, and $K_2 = 17.50$) for the irradiation model [4]. Direct irradiation (W/m^2) is given

$$\boldsymbol{I_N = I_{ON} e^{-m\,\varepsilon\,T_R + \alpha}} \tag{2-3}$$

where m and ε are dependent on zenith angle. Then, direct irradiation must be multiplied by $\cos(\theta_i)$ to find the component normal to the surface of interest (where θ_i is the incident angle to the surface, Figure 2-5). In the case illustrated in Fig. 2-4, the basin normal is vertical, so $\theta_i = \theta_z$.

2.3.2 Roof-type, Half-pyramid, and Single Slope Stills

Three types of still covers were treated in this study, as mentioned earlier.

All three covers were placed over a horizontal surface of arbitrary width (W) and length (L) which were assumed to be 1 meter each for the current analysis. The tilt angle of both the front face (oriented south) and the side faces of the single slope cover and roof-type cover could change during optimization, to the point where they would effectively become a half-pyramid. The other limiting case was where the tilt angles were 90° for the triangular side surfaces. The north oriented surfaces were all maintained vertical and not allowed to vary.

Ultimately the direct portion of radiation that gets through a cover surface becomes a projection of that shape to the basin. Another way of thinking about this is to pretend that a cover surface is replaced by an opaque surface, and the shadow falls on the ground where the projected area lies. The intersection of the shadow with the basin area is the area that has the potential to absorb direct radiation from the same cover surface. See Figures 2-6 to 2-8 for an illustration of this idea.

Points (x_1, y_1) and (x_2, y_2), shown in Figs. 2-9 to 2-11, are projections of the points corresponding to the elevated corners of a given face.

A triangular surface and a trapezoidal surface will leave different projected areas on the basin. Several different shapes are possible depending on the orientation of the sun. For the triangular surface, the equation that determines the projected basin area depends on which region the projected tip point falls within (Figure 2-9). As a result, there are six possible shapes and corresponding equations for the projected basin area. For example, the projected basin area in case 1 would be

$$\boldsymbol{A_{p,basin} = \frac{x_1 W^2}{2y_1}}. \qquad \textbf{(2-4)}$$

Deriving this expression is simply a matter of finding the intersection area. In this case, you can imagine two similar right triangles, one with a corner at (x_1,y_1), and one with a corner on the border of regions 1 and 6. The area of any triangle is given

$$\boldsymbol{A_{triangle} = \frac{1}{2} Height \cdot Base}, \qquad \textbf{(2-5)}$$

then the height can be found by the similar triangles,

$$\frac{y_1}{Height} = \frac{x_1}{W}. \tag{2-6}$$

Then, the base is simply W.

For a trapezoidal surface, the shape of the projected basin area requires the projection of two points. The shape formed on the basin depends sometimes on the position of one of the points and sometimes the other. There are a total of eight shapes possible and therefore eight equations. Case 1 for the trapezoid shows that the projected basin area would be

$$A_{p,basin} = \frac{x_2 W^2}{2y_2} \tag{2-7}$$

until the red lines shown in Figure 2-10 cross. Case 4 for the trapezoid shows that the projected basin area would be

$$A_{p,basin} = \frac{1}{2}L\left(2W + \frac{L(W+y_1)}{x_1}\right), \tag{2-8}$$

which holds as long as $\frac{-x_1}{W+y_1} \geq \frac{L}{W}, x_1 \leq -L \; and \; y_2 \geq 0$.

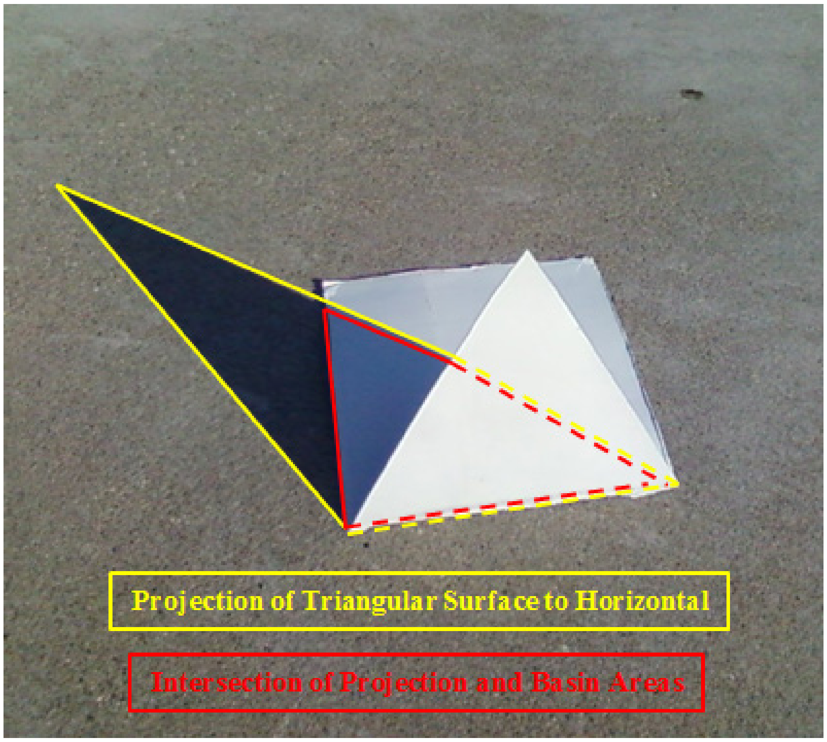

Figure 2-6: Illustration of the Projected Area on the Basin (Triangular Face Case 1)

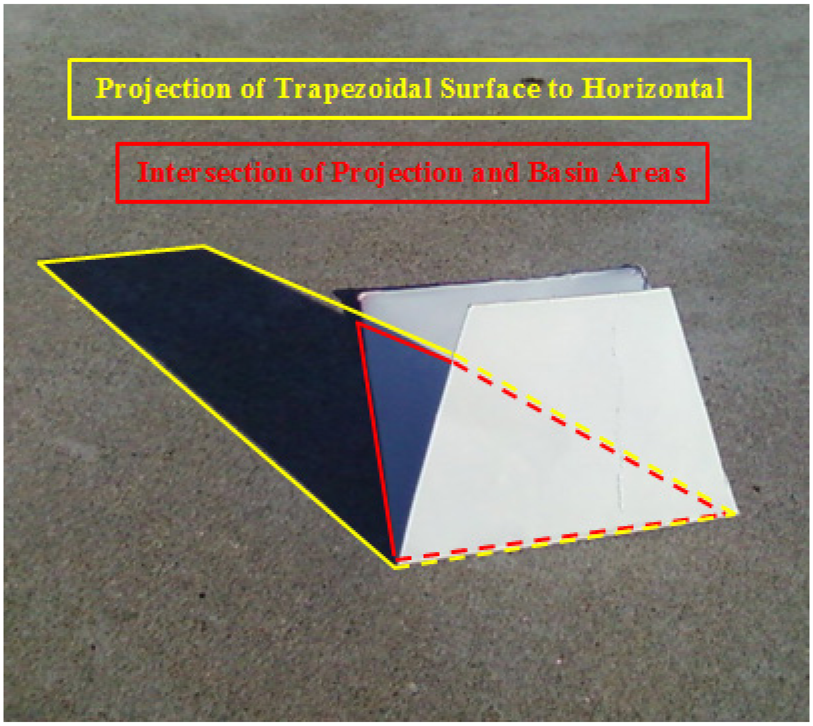

Figure 2-7: Illustration of the Projected Area on the Basin (Trapezoidal Face Case 1)

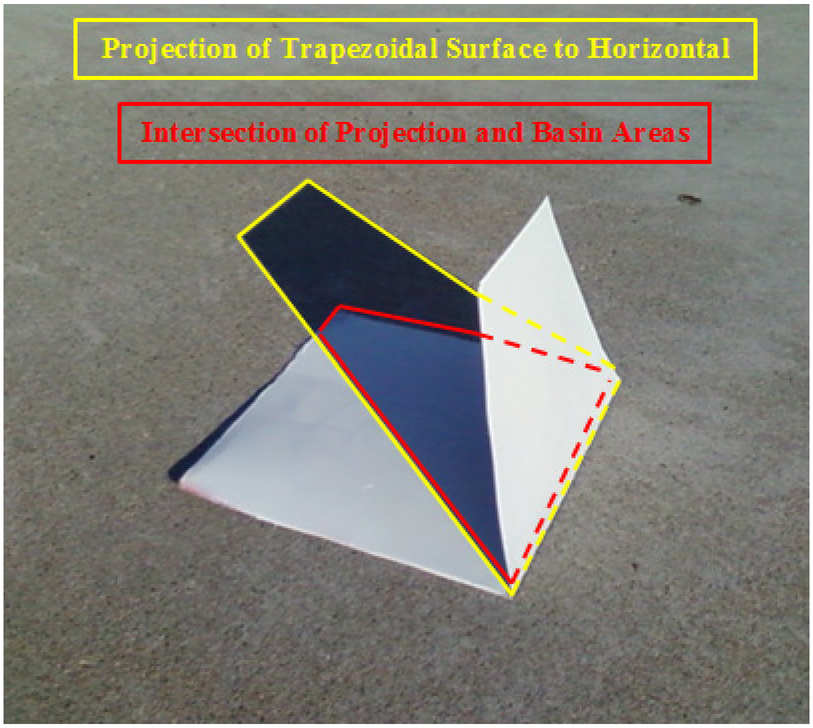

Figure 2-8: Illustration of the Projected Area on the Basin (Trapezoidal Face Case 4)

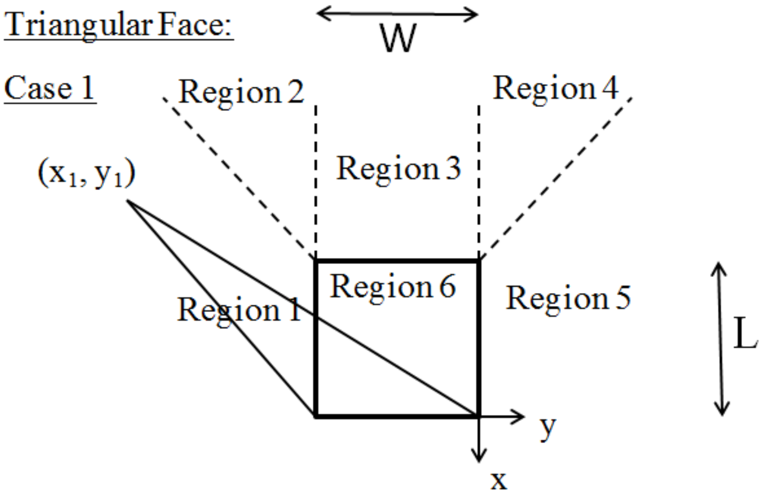

Figure 2-9: Projected Triangle

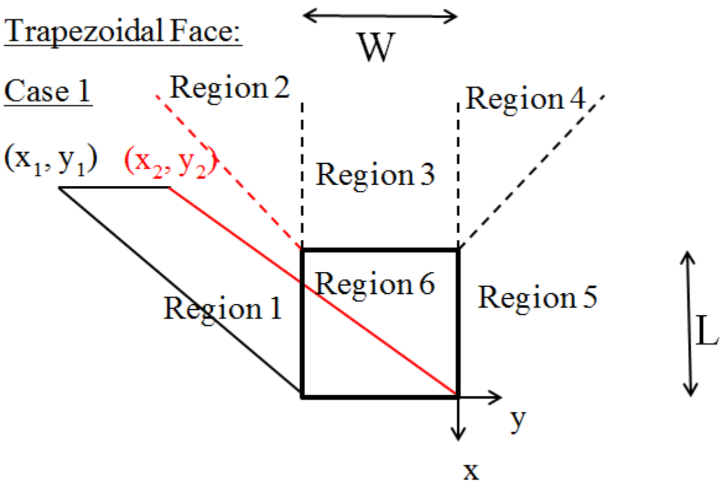

Figure 2-10: Projected Trapezoid

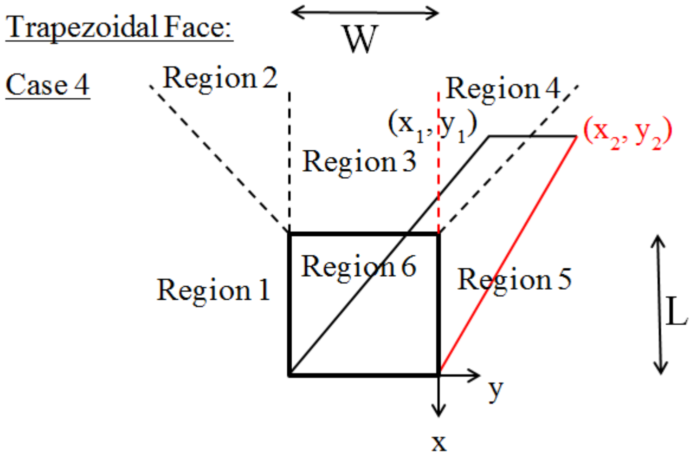

Figure 2-11: Projected Trapezoid

Table 2-1: Triangular Face Projected Areas

Case/Region	Area	Constraints
1	$A' = \frac{1}{2} WL \frac{x_1}{y_1} \frac{W}{L}$	$y_1 < -W, \frac{x_1}{y_1} < \frac{L}{W}$
2	$A' = \frac{1}{2} L \left(2W - \frac{y_1 L}{x_1} \right)$	$y_1 \leq -W, \frac{x_1}{y_1} \geq \frac{L}{W}$
3	$A' = \frac{1}{2} L \left(W + \frac{W(x_1 + L)}{x_1} \right)$	$0 > y_1 > -W, x_1 < -L$
4	$A' = \frac{1}{2} L \left(2W + \frac{L(y_1 + W)}{x_1} \right)$	$y_1 \geq 0, \frac{-x_1}{y_1 + W} \geq \frac{L}{W}$
5	$A' = \frac{1}{2} WL \frac{-x_1}{y_1 + W} \frac{W}{L}$	$y_1 > 0, \frac{-x_1}{y_1 + W} < \frac{L}{W}$
6	$A' = \frac{1}{2} (-x_1) W$	$0 \geq y_1 \geq -W, 0 \geq x_1 \geq -L$

Table 2-2: Trapezoidal Face Projected Areas

Case/Region	Area	Constraints
1	$A' = \frac{1}{2} WL \frac{x_2}{y_2}$	$y_2 \leq -W, \frac{x_2}{y_2} < \frac{L}{W}$
2	$A' = \frac{1}{2} L \left(2W - \frac{y_2 L}{x_2} \right)$	$x_1 \leq -L, y_1 \leq -W, \frac{x_2}{y_2} \geq \frac{L}{W}$
3	$A' = LW \left(1 - \frac{1}{2} \frac{y_2}{x_2} + \frac{1}{2} \frac{W + y_1}{x_1} \right)$	$0 > y_1 > -W, 0 > y_2 > -W,$ $x_1 < -L, x_2 < -L$
4	$A' = \frac{1}{2} L \left(2W + \frac{L(y_1 + W)}{x_1} \right)$	$x_1 \leq -L, y_2 \geq 0, \frac{-x_1}{y_1 + W} \geq \frac{L}{W}$
5	$A' = \frac{1}{2} WL \frac{-x_1}{y_1 + W}$	$y_1 \geq 0, \frac{-x_1}{y_1 + W} < \frac{L}{W}$
6	$A' = \frac{1}{2} (-x_2)(2W + y_2)$	$0 \geq y_2 \geq -W, 0 \geq x_2 \geq -L, y_1 < -W$
7	$A' = \frac{1}{2} (-x_2)(W + y_2 - y_1)$	$0 \geq y_2 \geq -W, 0 \geq x_2 \geq -L,$ $0 \geq y_1 \geq -W, 0 \geq x_1 \geq -L$
8	$A' = \frac{1}{2} (-x_2)(W - y_1)$	$0 \geq y_1 \geq -W, 0 \geq x_1 \geq -L, y_2 > 0$

2.3.3 Cover Material's Effect on the System

The cover material plays an important role. If the cover material didn't have directional properties (diffuse transmitter), the cover geometry wouldn't affect the radiation reaching the basin. However, this model was made to study the directional properties of the cover material and how they affect the total radiation reaching the basin.

For the preliminary study, the cover was assumed to be made of glass. After spectrally averaging the index of refraction, it was found that for solar radiation, glass has an average index of refraction of 1.458. It was also assumed that the attenuation coefficient of the glass was 1 x 10^{-4} m^{-1} for the solar spectrum. The glass was assumed to be 5 mm thick for every surface.

As found in the literature [21], the cover was modeled using electromagnetic wave theory. Using the index of refraction, the reflectivity was defined

$$\rho = \frac{1}{2}\left[\frac{sin^2(\theta-\chi)}{sin^2(\theta+\chi)} + \frac{tan^2(\theta-\chi)}{tan^2(\theta+\chi)}\right] \tag{2-9}$$

$$where\ \chi = \begin{cases} sin^{-1}(n\,sin\,\theta)\ for\ n\,sin\,\theta \le 1 \\ 0\ for\ n\,sin\,\theta > 1 \end{cases}$$

The absorptivity and transmissivity are then given

$$\alpha = 1 - \rho - \tau\ and\ \tau = e^{-\frac{\kappa t}{\cos\chi}} \tag{2-10}$$

where t is the thickness of the cover, and κ is the attenuation coefficient [22].

For a finite slab of semitransparent material, the effective reflection, absorption, and transmission coefficients were needed. From Siegel and Howell [22], the effective transmission coefficient is

$$T = \frac{\tau(1-\rho)(1-\rho^2)}{(1+\rho)(1-\rho^2\tau^2)}, \tag{2-11}$$

the effective reflection coefficient is

$$R = \rho(1 + \tau T)\,, \tag{2-12}$$

and the effective absorption coefficient is

$$A = \frac{(1-\rho)(1-\tau)}{(1-\rho\tau)}. \tag{2-13}$$

2.3.4 Energy Balance and Resulting Heat Transfer

Now that the solar angles, the solar irradiation, the projected basin areas, and the transmission coefficients are known for each of the cover surfaces, the total radiation ($q_{solar,total}$) to the basin was found (index i represents the surface).

$$\boldsymbol{q_{solar,total} = \sum_{i=1}^{4} I_N T_i A_i' \cos\theta_z = I_N \cos\theta_z \sum_{i=1}^{4} T_i A_i'} \qquad \textbf{(Watts)} \qquad \textbf{(2-14)}$$

2.4 Optimization Process

For the optimization process, the total solar radiation to the basin ($q_{solar,total}$, W) was integrated over the entire day to find the total energy absorbed, $Q_{solar,total}$ (MJ). This predicted which cover performed the best in terms of total energy absorbed by the basin (in this model, the basin was simply assumed to be black).

2.4.1 Excel Radiation Model

Microsoft Excel 2010 was used to make a spreadsheet that calculated the total daily energy absorbed. The results of $q_{solar,total}$ were integrated numerically with the trapezoid rule and a step size of 60 seconds to yield $Q_{solar,total}$. The optimization was done using Excel's solver add-in.

Table 2-3: Optimization Problem Summary

<table>
<tr><th colspan="2">Optimization Problem Setup</th></tr>
<tr><td colspan="2">Find the values of θ and φ that maximize $Q_{solar,total} = \int_0^{24\ hours} I_N \cos\theta_z \sum_{i=1}^{4} T_i A_i' \, dt$
where $I_N = f(t)$ (see equation 2-3)
$\theta_z = f(t)$ (see equation 2-2)
$\theta_i = f(\theta_{cover}, \varphi_{cover}, t) = \cos^{-1}(\hat{n}_{sun} \cdot \hat{n}_{surface,i})$
$T_i = f(\theta_i)$ (see equation 2-11)
$A_i = f(\theta_{cover}, \varphi_{cover}, t)$ (see Tables 2-1 and 2-2)</td></tr>
<tr><th>Single Slope Constraints</th><th>Roof Type/Half-Pyramid Constraints</th></tr>
<tr><td>$W = 1\, meter$
$L = 1\, meter$
$1° \leq \theta \leq 89°$
$1° \leq \varphi \leq 90°$
$\frac{2H}{\tan\varphi} < W$</td><td>$W = 1\, meter$
$L = 1\, meter$
$1° \leq \theta \leq 90°$
$1° \leq \varphi \leq 89°$
$\frac{H}{\tan\theta} \leq L$</td></tr>
</table>

2.4.2 Optimization Setup

The model was set up to vary each geometry according to the constraints given in section 3.2 above. GRG nonlinear algorithm was chosen. Automatic variable and objective scaling was used to keep the optimization process as simple as possible. Forward difference approximation was used for calculation of all derivatives. Once the geometric constraints were properly added, the solver iterated until reaching the global maximum (depending on the starting point, usually less than 10 iterations were required). To verify the global maximums, the design spaces and optimums are shown in Figures 2-12 and 2-13. Table 2-3 shows the setup of the optimization problem.

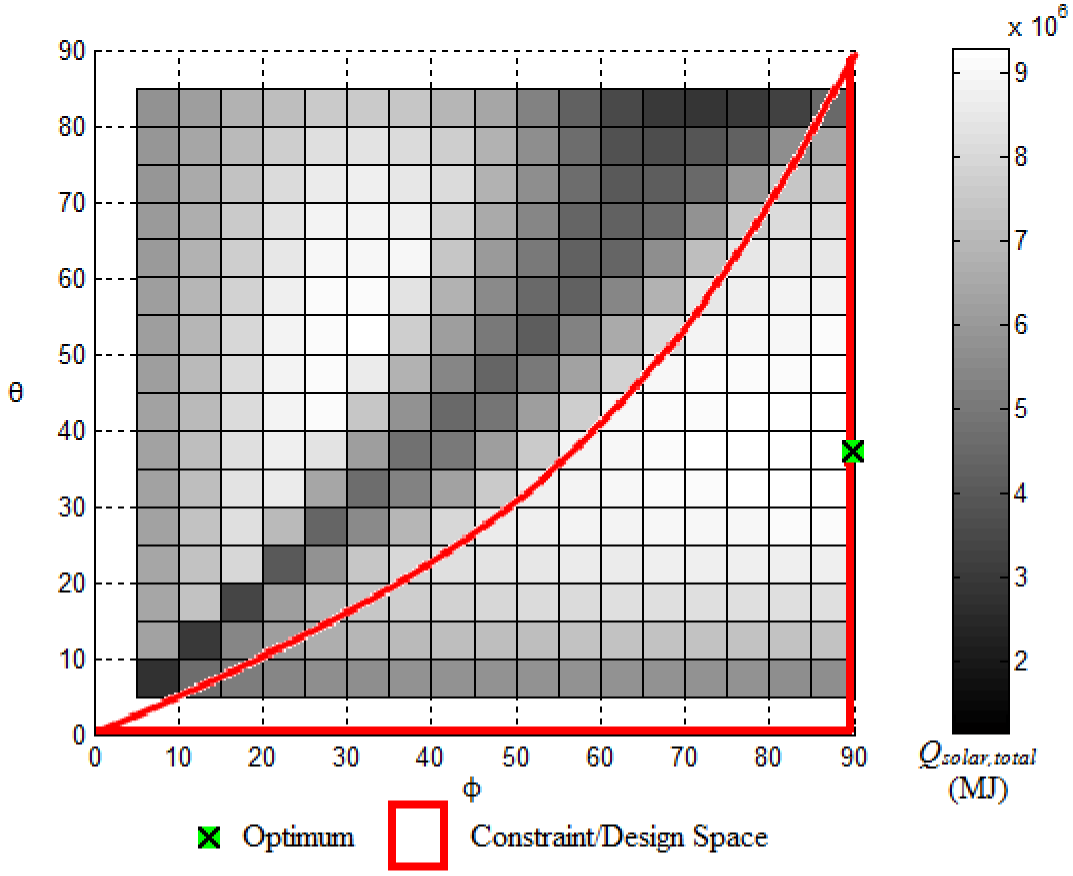

Figure 2-12: Design Space of Single Slope Still

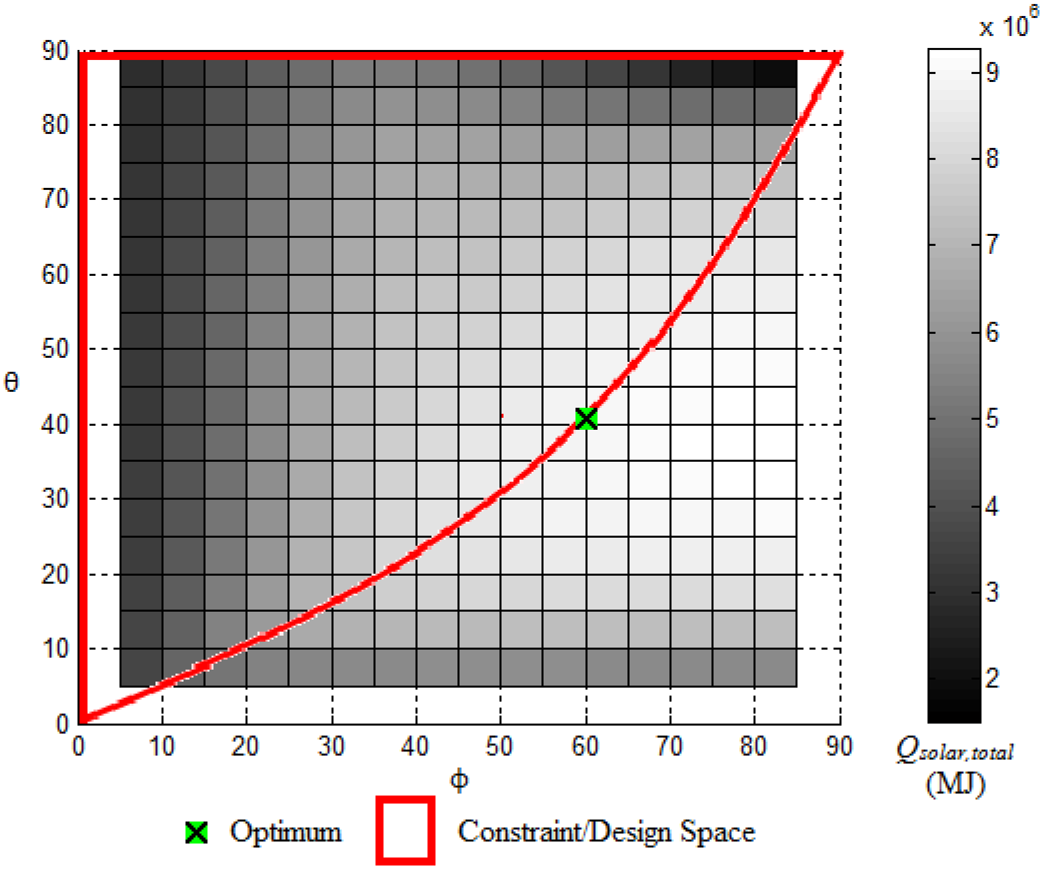

Figure 2-13: Design Space of Roof Type/Half-Pyramid Still

2.5 Optimization Results

In order to give the production model some validation, a similar pyramid and single slope still were modeled in MATlab under Aswan solar conditions to compare with values from Fath [10]. The model yielded 2.41 L/m^2 per day for a pyramid similar to Fath's geometry, and 2.79 L/m^2 per day for a single slope still with the same geometry and setup as Fath's. These results all fall within ±7.3% of Fath's results. Using these tuned results, estimates were generated for Utah's climatic conditions during the autumnal equinox. Assuming the optimized cover geometries, the half-pyramid would produce 1.36 L/m^2 and the single slope would produce 1.23 L/m^2 (within 10% of each other).

2.5.1 Geometries that Performed the Best

The geometry that outperformed all the others in terms of radiation reaching the basin was the single slope cover (wedge). The pyramid was not far behind, only about 3.9% less radiation arrived at the basin for the pyramid shape. Geometries resembling the roof type cover were generally unfavorable because reflective losses were higher than the other geometries. The initial geometries chosen show this general trend (Figure 2-14, Table 2-4).

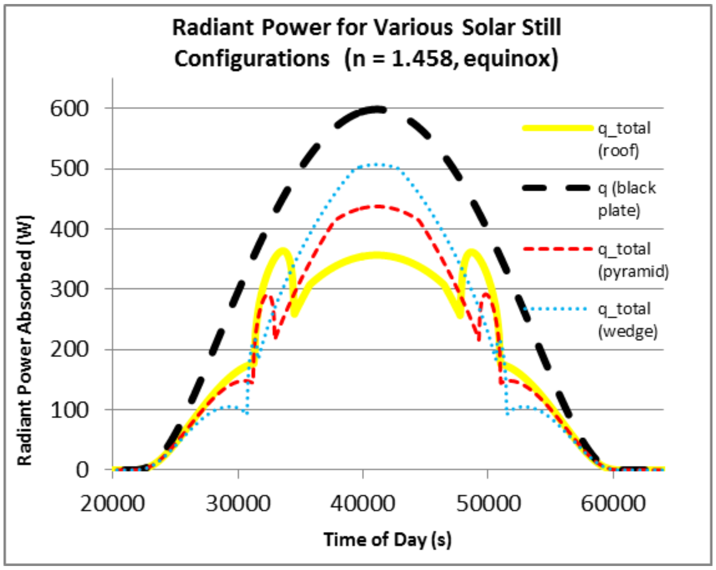

Figure 2-14: Initial Solar Still Configurations

Table 2-4: Initial Solar Still Configurations

Still Type	South Face Tilt (°)	East/West Face Tilt (°)	Energy Absorbed by Basin (MJ)
Roof	57.3	60.2	8.04
Pyramid	56.3	71.6	8.41
Wedge	45	80.2	8.92

2.5.2 Final Optimized Cover Geometries

All three cover optimization processes produced valuable results for getting the best cover geometry (in terms of radiation). The side faces of the single slope cover became vertical, and the south face tilted at an angle of 37.1°. This shows that the south face contributes the most to the total radiation hitting the basin.

The half-pyramid only changed its height, since the faces were all constrained to meet at a point. The side angles converged to 60.6° with the horizontal and the south face tilted at 41.5° at the end of the optimization.

The roof type cover aligned its south face to 41.5°, and then the height of the still increased until the sides became triangles. The side faces were tilted at 60.6° at the end of the optimization process, so essentially it evolved to become identical to the half-pyramid. The optimizations were performed for winter and summer solstices as well, see Table 2-5.

2.5.3 Visualization of Results

The results of the optimization study are shown in Figure 2-15. The radiant power absorbed by an uncovered black plate is shown, along with the optimized single slope, half-pyramid, and roof type covers. Note that while the peak of the optimized single slope is higher, the optimized pyramid is broader. The dips represent where the direct radiation reaches the Brewster angle for one or more of the surfaces. Overall, there is slightly more area under the single slope's curve than the pyramid's or roof's curve. Figures 2-16 and 2-17 show the two optimum cover geometries for the Provo, Utah conditions described previously.

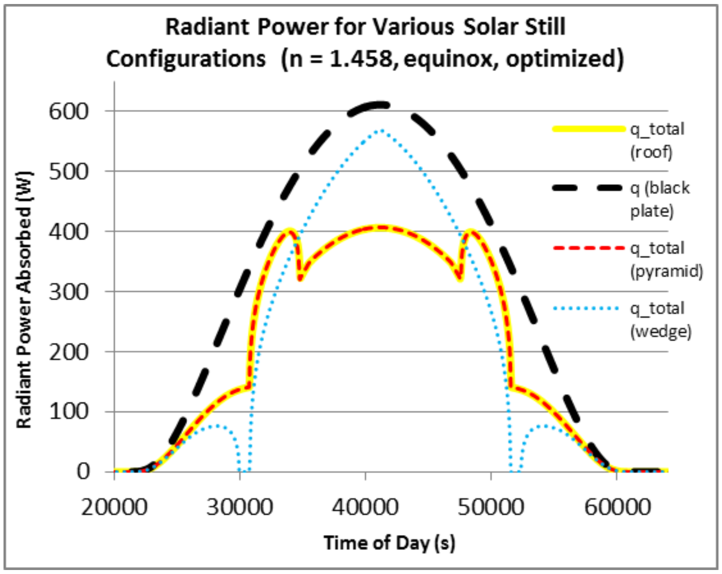

Figure 2-15: Optimized Solar Still Configuration

Table 2-5: Optimized Solar Still Configurations

Still Type	Season	South Face Tilt (°)	East/West Face Tilt (°)	Energy Absorbed by Basin (MJ)
Roof	Vernal Equinox	41.6	60.6	8.98
	Summer Solstice	17.2	31.8	15.8
	Autumnal Equinox	42.4	61.3	8.68
	Winter Solstice	84	78	2.45
	Average	46.3	57.925	8.9775
Pyramid	Vernal Equinox	41.5	60.6	8.98
	Summer Solstice	18.4	33.6	15.8
	Autumnal Equinox	42.1	61.1	8.68
	Winter Solstice	83.8	77.8	2.45
	Average	46.45	58.275	8.9775
Wedge	Vernal Equinox	37.1	90	9.34
	Summer Solstice	16.1	90	15.8
	Autumnal Equinox	37.2	90	9.05
	Winter Solstice	59.4	90	2.56
	Average	37.45	90	9.1875

2.6 Conclusion of Optimization Results

For the optimization of solar radiation absorbed, the optimized single slope cover performed better than the optimized half-pyramid, but the difference in total energy absorbed was about 3.9%.

2.6.1 Implications for Engineers

For solar distillation, a single slope cover and a half pyramid cover will perform nearly the same. As a result, output of each will be nearly the same.

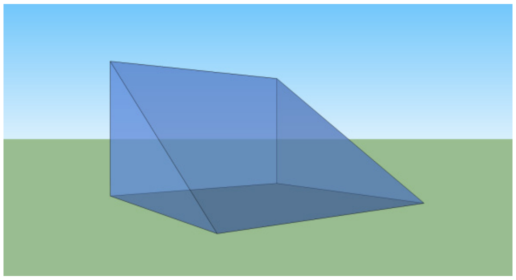

Figure 2-16: Optimized Single Slope

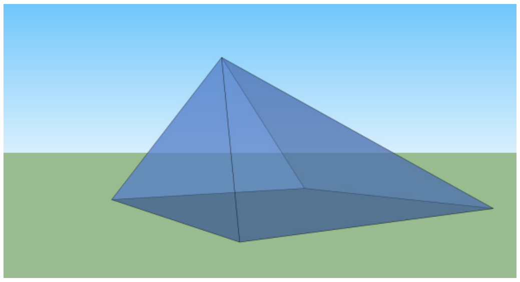

Figure 2-17: Optimized Half-Pyramid/Roof Type

2.6.2 Suggestions for Future Research

The model described in this article gives a reasonable approximation of the radiation arriving at the basin, but the model neglects the effects of internal reflections. As radiation coming in one face of the cover eventually arrives at another cover surface, a portion of that radiation will be transmitted and another portion will be reflected back to another face of the cover or even the basin. This would probably increase the amount of radiation arriving at the basin, and should be considered as a topic of future studies. Also, future efforts could include the effects of varied weather conditions, as cloudy conditions increase diffuse radiation and decrease the direct component. This could yield a different optimized geometry when cover to basin viewfactors are taken into consideration. Finally, a convection model that accurately takes into account the possible variations in still cover geometry could yield more accurate results for predicting the actual production.

3 NUMERICAL SIMULATION OF CONVECTION IN TRIANGULAR CAVITIES TO PREDICT SOLAR STILL PERFORMANCE[3]

3.1 Introduction and Literature Review

Accurately calculating the heat and mass transfer within a solar still is always of interest to designers of solar stills. Without accurate convection correlations, there cannot be accurate predictions of the total distillation (using the heat and mass transfer analogy). The heat and mass transfer analogy can be related using the Lewis number, thermal conductivity, and mass diffusivity. The relationship is given

$$h_m = h\frac{D_{AB}Le^n}{k}. \qquad \textbf{(3-1)}$$

One of the first to study convection in cavities as it relates to solar distillation was Dunkle, who found C = 0.075 and n = 1/3 for a correlation of the form

$$Nu = C \cdot (GrPr)^n = C \cdot Ra^n \text{ [23]}. \qquad \textbf{(3-2)}$$

Clark came up with a similar correlation, except he extended the range to cover lower Grashof Numbers and divided the coefficients into laminar and turbulent regions [24]. Shawaqfeh and Farid found a fit with C = 0.067 and n = 1/3, also very similar to Dunkle's results. Kumar and Tiwari used regression to find C = 0.0322 and n = 0.4144 for Grashof numbers ranging in the millions [25]. Finally, probably the most extensive work for triangular cavities was completed by Shruti and Tiwari, in which coefficients were found for triangular geometries at 15°, 30°, and

---

[3] Chapter submitted for publishing in *Desalination*.

45° [26, 27]. Table 3-2 summarizes coefficients and Grashof ranges for the mentioned works. The characteristic length for these correlations is defined as

$$\boldsymbol{L_C = \frac{\forall}{A_b} = \frac{H}{2}} \tag{3-3}$$

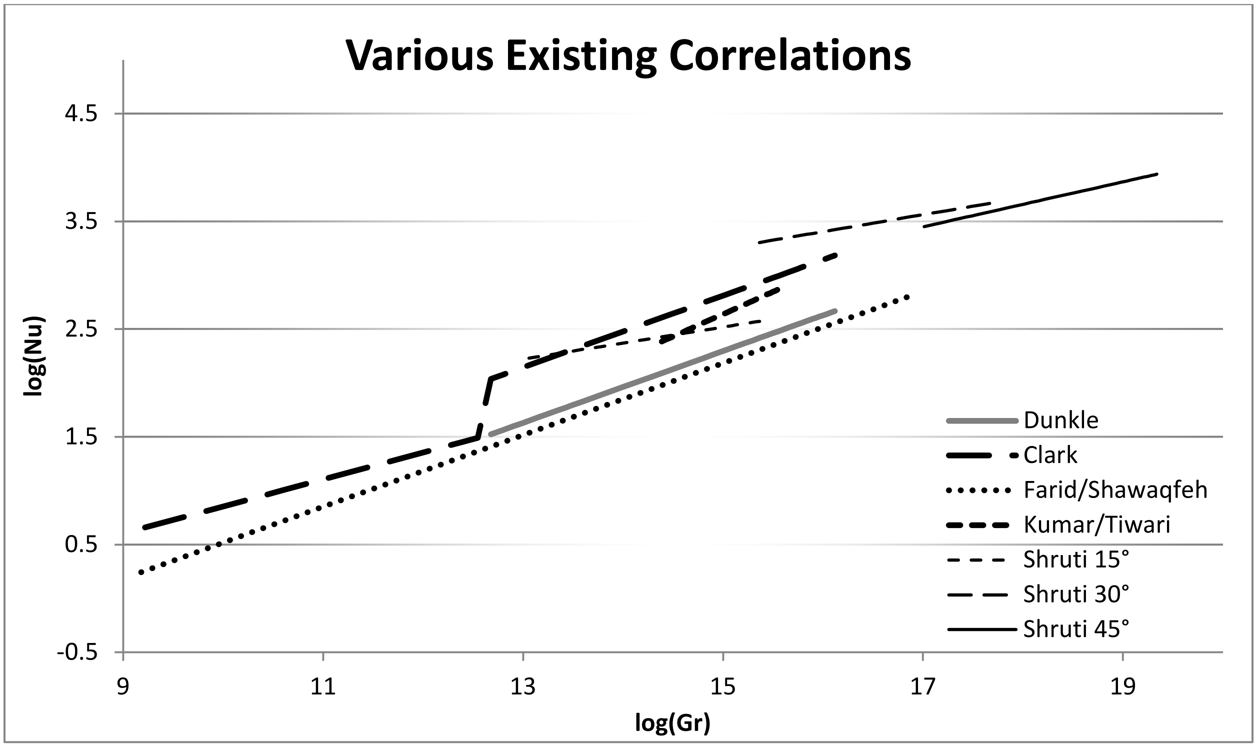

Figure 3-1: Comparison of Existing Convection Correlations

While there are multiple correlations that have been developed for predicting the convection and mass transfer coefficient, they are not always in good agreement (see Figure 3-1) and some have limited Grashof number range. For example, Shruti's correlations predict higher Nusselt number at higher Grashof numbers than all the other correlations. On the other hand, Farid and Shawaqfeh predict lower values of Nusselt over a wide range compared to all other correlations. All of the previous correlations were experimentally measured using specific cover geometries, and may be less accurate for cover geometries that are different than the original cover for which they were developed. As a result, it is desirable to develop a correlation that can be used over a wide range of geometries and Grashof numbers. The current approach, like Shruti's, will account for changes in cover geometry and extend the range of Grashof numbers compared to earlier correlations. CFD is an obvious choice when data is desired without having to build a prototype or purchase data acquisition hardware.

In the paper that follows, the geometries studied will first be defined. Next, the numerical grid and solution process will be described. Lastly, the results of the simulation will be presented and compared to the correlations presented above.

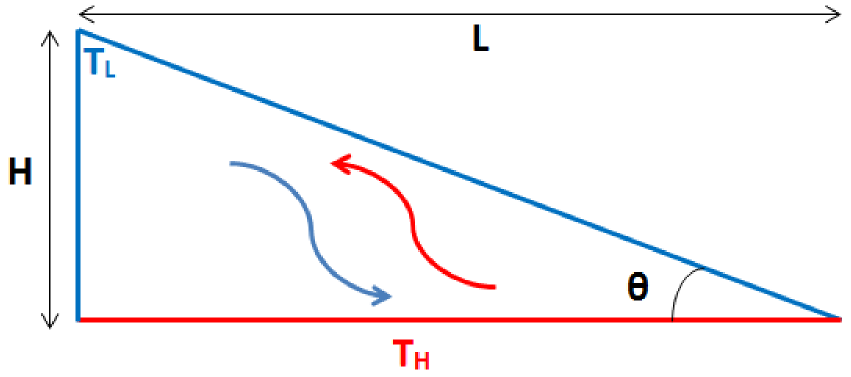

Figure 3-2: Geometry and Dimensions of Triangular Cavity

3.2 Geometries Studied

The current study modeled right triangle cavities at angles of 15°, 30°, and 45°. The reason for studying different geometries is due to changes in the flow with changes in the tilt angle. These changes are due to the fact that the flow is impeded near the sharp corner of the still, where the eddies are inhibited by the meeting of the two walls. As the mentioned impediment is reduced by higher angles, the eddies are allowed to constructively interfere with each other and direct the flow upward more easily where they meet.

Isothermal boundary conditions were assumed. However, a small (1e-4 m) adiabatic surface was created to separate the isothermal boundaries and avoid discontinuities at the intersection of the two isothermal boundaries. Dimensions of the cavities were L = 1 m and H = tan(θ) m. See Figure 3-2 for an illustration of the geometry's setup. To minimize calculation time while still maintaining some accuracy to the experimental data, a 2D cavity was chosen.

3.3 CFD Setup and Simulation

3.3.1 Mesh Creation

Geometries were created and meshed in Gambit version 2.3.16. Five surfaces were created, two representing the two cover surfaces at temperatures of T_L, one representing the surface of the basin at a temperature of T_H, and two adiabatic regions were added to avoid discontinuities at the corners. During the meshing process, a sizing function was used to scale the node spacing to the order of the shortest lengths near the shortest adiabatic surfaces. The sizing function was tied to those points with a characteristic size 0.0001 m, a maximum size 0.01 m, and a growth rate of 1.15. Then, the surfaces and fluid were meshed using triangular elements to reduce false diffusion. The mesh was then exported for use in Fluent 12. The 15° case started at 2559 nodes, the 30° case started at 4376 nodes, and the 45° case started at 7311 nodes. See Figure 3-3 for an example of the mesh.

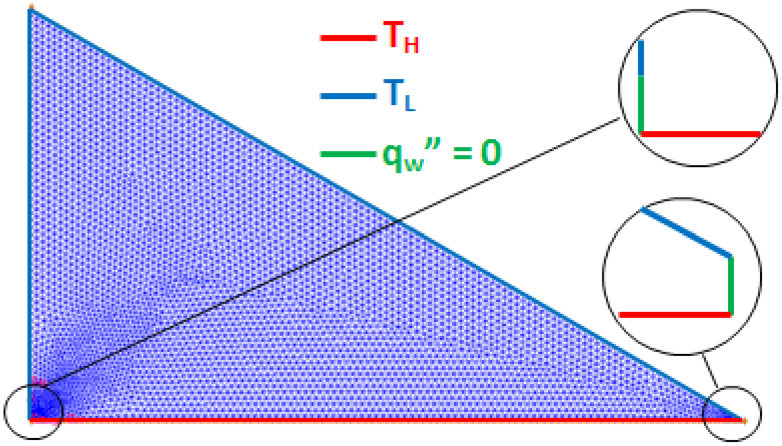

Figure 3-3: Mesh as Created in Gambit for 30° Triangle

3.3.2 Setup in CFD Package

As mentioned, Fluent 12 was used to setup and find a solution to the fluid problem. Before running the fluid simulation, the energy equation was used to solve for the case in which heat transfer occurs only via conduction (the effects of gravity were turned off in the model). The total heat transfer was iterated until the surface monitors (heat flux integrated over the various surfaces) converged and the mesh was refined by temperature until grid independence was found. The refined mesh was then used for solving the actual convection cases. The pressure based solver was selected; SIMPLE pressure-velocity coupling was used. To do the convection calculations, gravity was turned on ($g=9.81\ m/s^2$). The RSM (Reynolds Stress Model) was selected for the calculation of the viscosity, as simulations performed seemed to show the best agreement with existing correlations. T_L was held constant at 285 K while T_H was varied from 285.01 to 385 K. Running simulations using different temperature differences generated results at different values of Grashof number. Properties were assumed to be close to those of dry air, as they were already in good agreement (less than 2% error for all properties) with Tiwari's calculation of humid air properties for the film temperature range [4].

$$T_{film} = \frac{T_H+T_L}{2} \tag{3-4}$$

$$k = .0031 + T_{film} \cdot 7.7 \cdot 10^{-5} \tag{3-5}$$

$$\begin{aligned} c_p = {} & 1161.482 - 2.368819 \cdot T_{film} + .01485511 \cdot {T_{film}}^2 \\ & -5.034909 \cdot 10^{-5} \cdot {T_{film}}^3 + 9.928569 \cdot 10^{-8} \cdot {T_{film}}^4 \\ & -1.111097 \cdot 10^{-10} \cdot {T_{film}}^5 + 6.540196 \cdot 10^{-14} \cdot {T_{film}}^6 \\ & -1.573588 \cdot 10^{-17} \cdot {T_{film}}^7 \end{aligned} \tag{3-6}$$

$$\rho = \frac{P}{R_{air} T_{film}} \tag{3-7}$$

$$\mu = \mu_{ref} \left(\frac{T_{film}}{T_{ref}}\right)^{3/2} \frac{T_{ref}+S}{T_{film}+S} \tag{3-8}$$

Once all the parameters were set, the solution was run for each case and data was collected.

3.4 Grid Dependence

As mentioned above, grid independence was found for the conductive heat transfer problem for each geometry, and an example is shown in Figure 3-4. As can be seen in Figure 3-4, by about 10,000 nodes, the solution was within 1% of the grid independent solution. The nearly grid independent meshes were then used to solve the convective problem. Due to limits on time, hardware resources, and software licenses, grid independence was not studied for the convective problem. However, the case where θ = 30° and ΔT = 1K was refined according to velocity and turbulent viscosity gradients. The error was estimated by comparing the value of the convective heat transfer for the coarse grids to that of the refined. It was found that up to 37%

error was possible using the coarser grid instead of the refined grid. Figure 3-5 shows the result of the grid dependence study for the θ = 30°, ΔT = 1 K case.

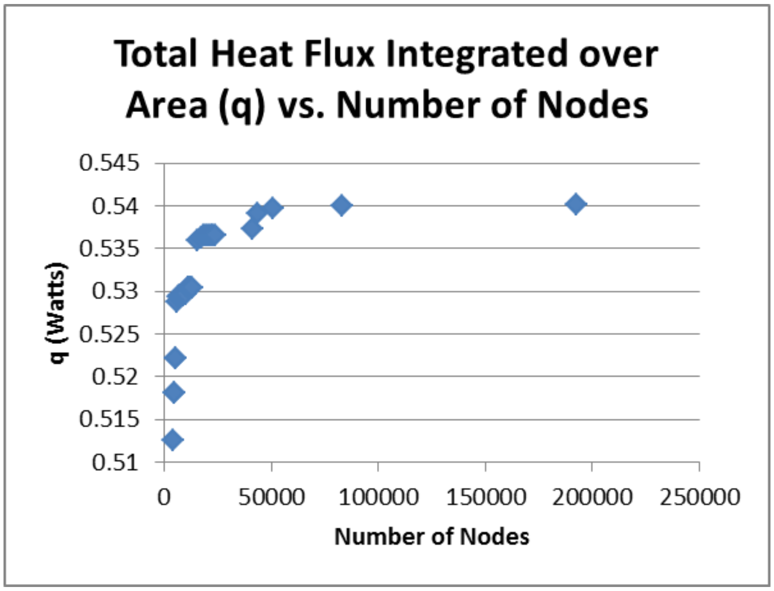

Figure 3-4: Grid Dependence for Conductive Heat Transfer (ΔT = 1 K, θ=30°)

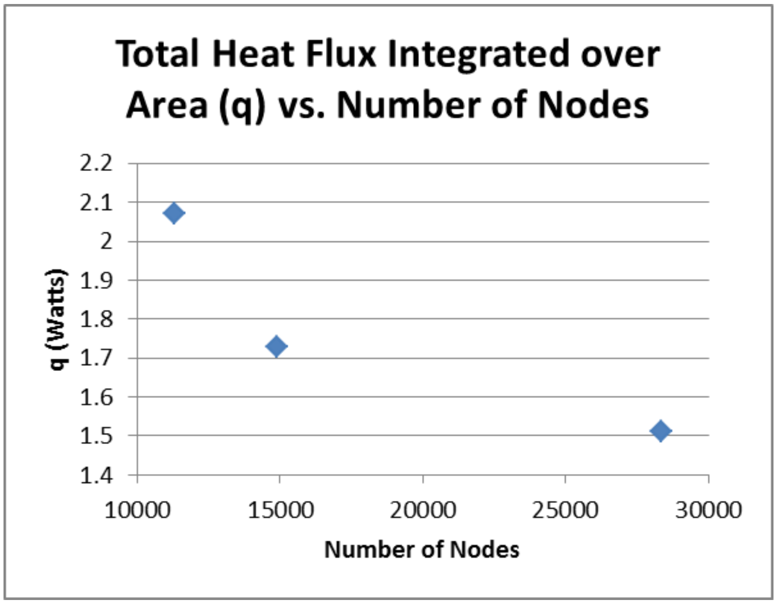

Figure 3-5: Grid Dependence for Convective Heat Transfer (ΔT = 1 K)

3.5 Results

At the end of the simulations, the data was gathered in a spreadsheet for evaluation. Table 3-1 and Figure 3-6 summarize the results. One goal of the research was to extend the range of Grashof numbers over which a correlation was available, so the basin temperature was varied logarithmically as shown in Table 3-1. Using Shruti's experimental work [26], error and Grashof number ranges were estimated for his varied tilt angle correlation (about 21.1% error). Similar estimates for Grashof range were made from Farid and Shawaqfeh's article [25]. Figure 3-7 shows this work's CFD results, nearly paralleling Shruti's model. Figure 3-8 (for the 30^{o} tilted cover plate) shows some disagreement between Shruti's correlation and CFD data, but within the estimated error bounds. Figure 3-9 (for the 45^{o} tilted cover plate) again shows the parallel behavior for Shruti's results and the CFD results given here. Figure 3-6 shows the general trend where cavities with lower cover tilt angles occupy a space with lower Nusselt numbers. Dunkle's correlation predicts Nusselt numbers approximately 35% to 55% lower than the CFD results (Figure 3-10). Farid's also seems to underestimate the Nusselt numbers (Figure 3-12). Clark's model (Figure 3-11) agrees well with the CFD for the higher range of Grashof numbers in the turbulent region. Kumar and Tiwari's model (Figure 3-13) seems to also occupy a region very near the CFD results. After considering the correlations mentioned, it was found that Shruti's correlations matched the CFD results better than the others (see Figures 3-7 to 3-9). Since the other correlations failed to capture the effects of changing the tilt angle, it's logical to assume that Shruti's correlation is the most accurate. The deviation between Shruti's results and the CFD results is still fairly high, but two possibilities could give an explanation: 1. The actual still covers used to collect experimental data by Shruti were three dimensional and finite, whereas the CFD simulation was for a two dimensional enclosure (which implies an infinite cover). 2. The actual single slope stills constructed by Shruti appear to have been trapezoidal cavities rather than triangular cavities [26, 27], which would cause some deviation due to the added gap between the basin and cover. The CFD data presented here was used to generate correlation coefficients which are given in Table 3-2.

Note that these correlations should mainly be used in solar stills that resemble triangular cavities, as error increases with deviations from the assumed geometry. Further work should be done to find valid correlations for angles greater than 45° or less than 15°. With further data, the correlation coefficients themselves could be modeled as functions of the tilt angle.

Table 3-1: CFD Results

15°		30°		45°	
T_{cover} (K)	q (Watts)	T_{cover} (K)	q (Watts)	T_{cover} (K)	q (Watts)
285.01	9.57E-03	285.01	6.36E-03	285.01	6.05E-03
285.1	1.27E-01	285.1	9.96E-02	285.1	1.14E-01
286	2.09E+00	286	1.673	286	2.13E+00
295	3.32E+01	295	3.55E+01	295	3.62E+01
335	2.23E+02	335	2.23E+02	335	2.38E+02
385	5.07E+02	385	5.07E+02	385	5.43E+02

Table 3-2: Correlation Coefficients and Details

Author(s)	Year	C	n	Valid Range
Dunkle	1961	0.075	1/3	$3.2 \times 10^5 < Gr < 10^7$
Clark	1990	0.21 0.1255	1/4 1/3	$10^4 < Gr < 2.5 \times 10^5$ $2.51 \times 10^5 < Gr < 10^7$
Shawaqfeh/Farid	1995	0.067	1/3	$1.6 \times 10^5 < Gr < 2.2 \times 10^7$ (estimated)
Kumar/Tiwari	1996	.0322	0.4144	$1.794 \times 10^6 < Gr < 5.724 \times 10^6$
Shruti	1999	1.418 2.536 0.968	0.148 0.158 0.209	$\theta = 15°$, $4.7 \times 10^5 < Gr < 4.8 \times 10^6$ $\theta = 30°$, $4.7 \times 10^6 < Gr < 4.8 \times 10^7$ $\theta = 45°$, $2.5 \times 10^7 < Gr < 2.5 \times 10^8$ (estimated)
Current Work	2012	1.0 0.56 0.66	0.19 0.24 0.24	$\theta = 15°$, $4.0 \times 10^3 < Gr < 1.9 \times 10^7$ $\theta = 30°$, $4.0 \times 10^4 < Gr < 1.9 \times 10^8$ $\theta = 45°$, $2.1 \times 10^5 < Gr < 1.0 \times 10^9$

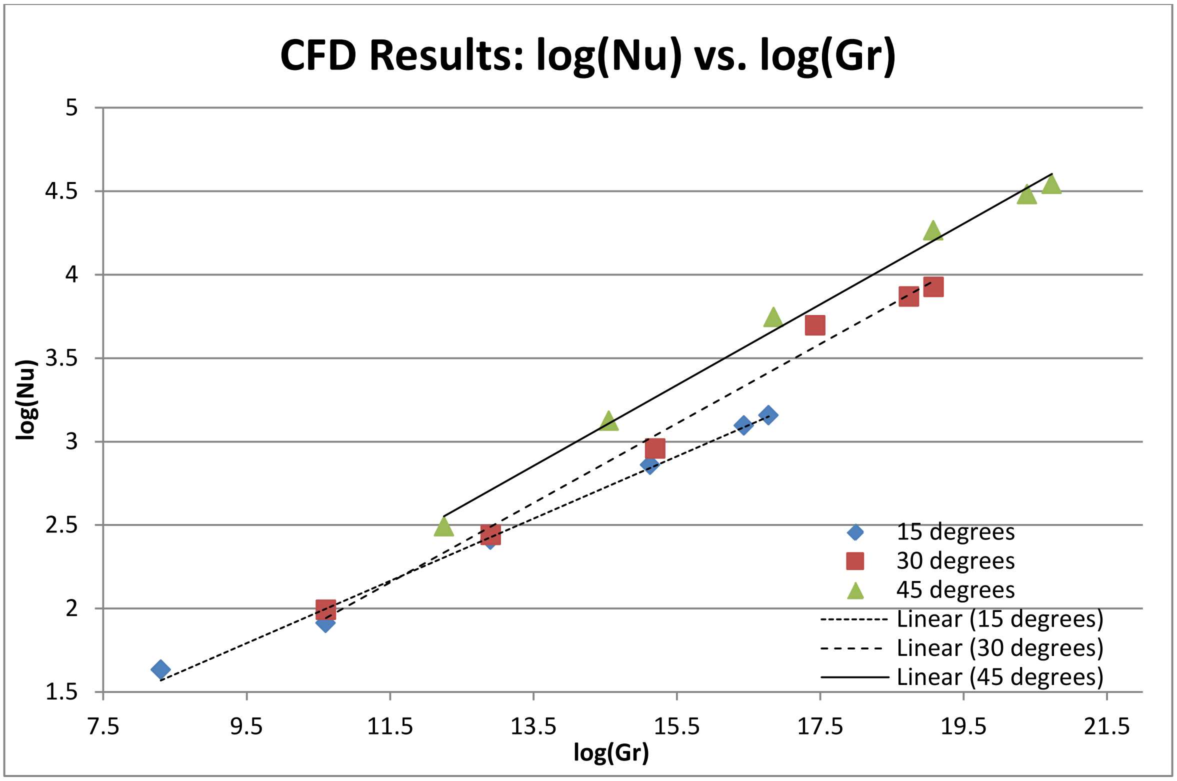

Figure 3-6: Comparison of CFD Data with Proposed Correlations for 15°, 30°, and 45°

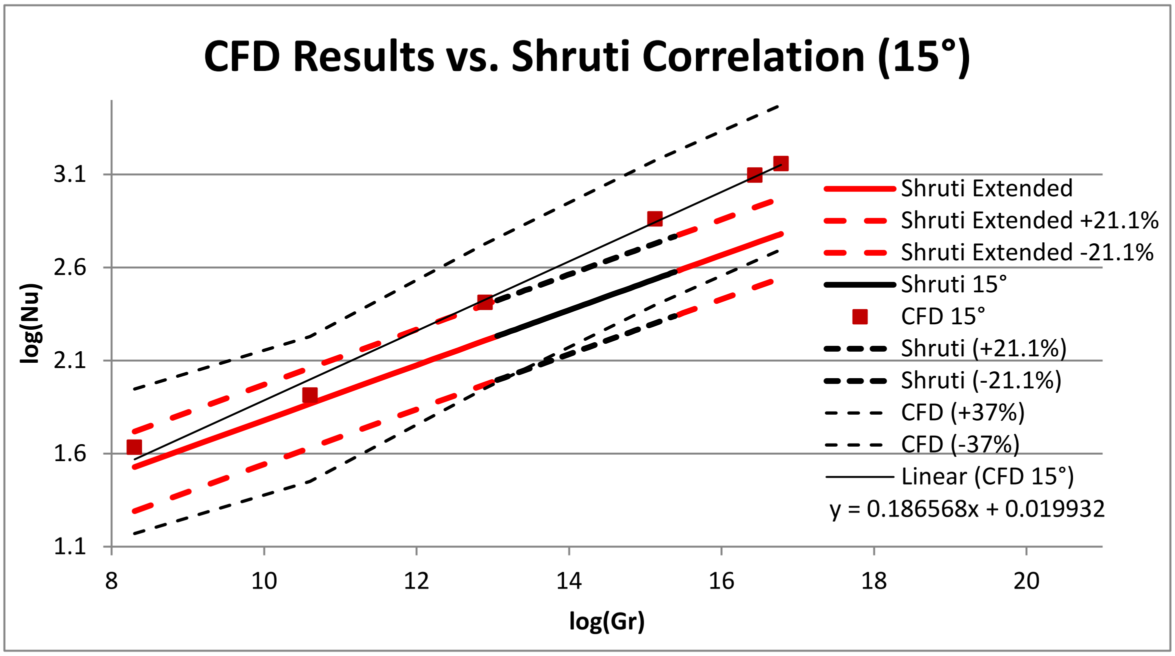

Figure 3-7: Comparison of Shruti's Correlation with CFD Data (15°)

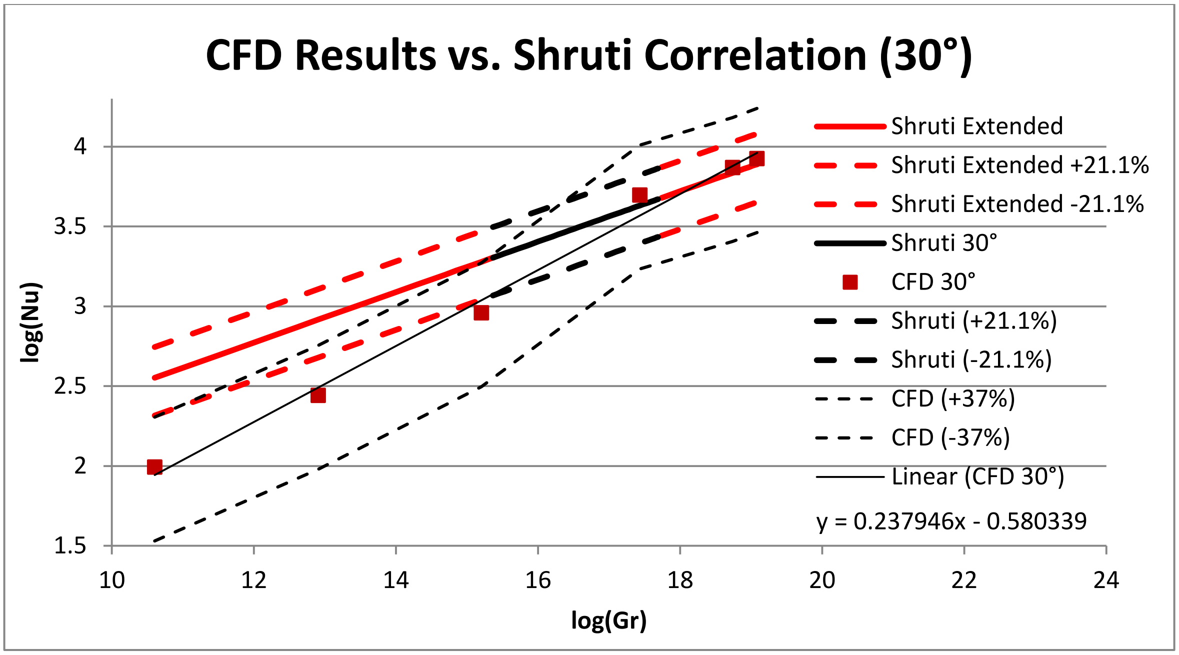

Figure 3-8: Comparison of Shruti's Model with CFD Data (30°)

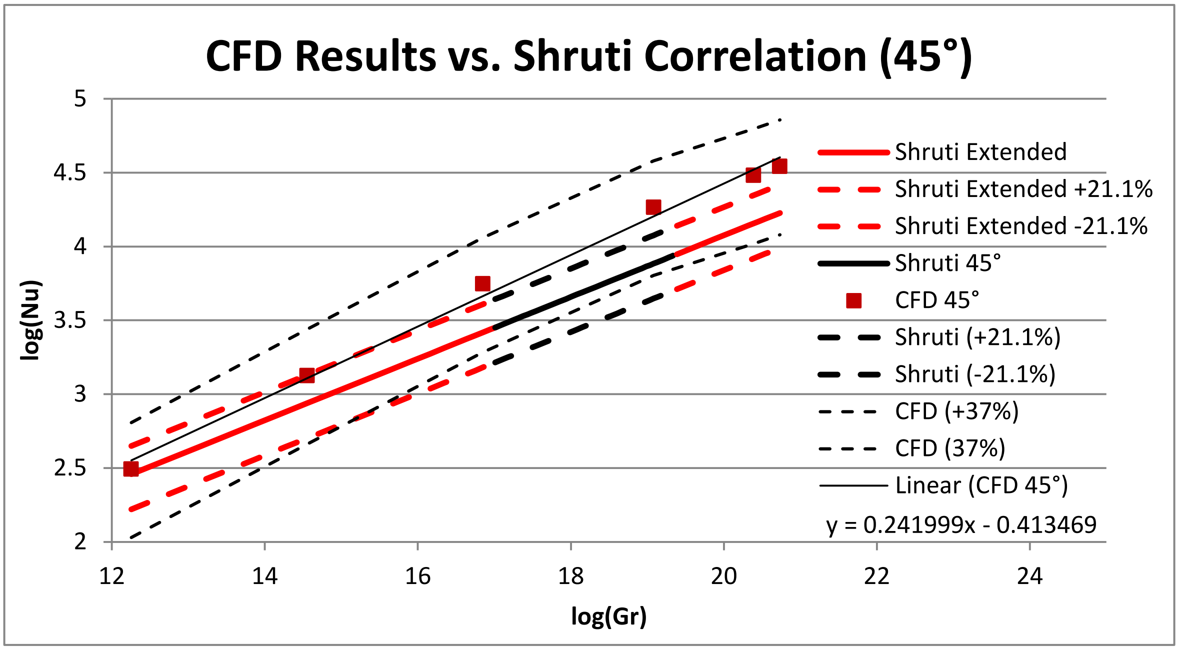

Figure 3-9: Comparison of Shruti's Correlation with CFD Data (45°)

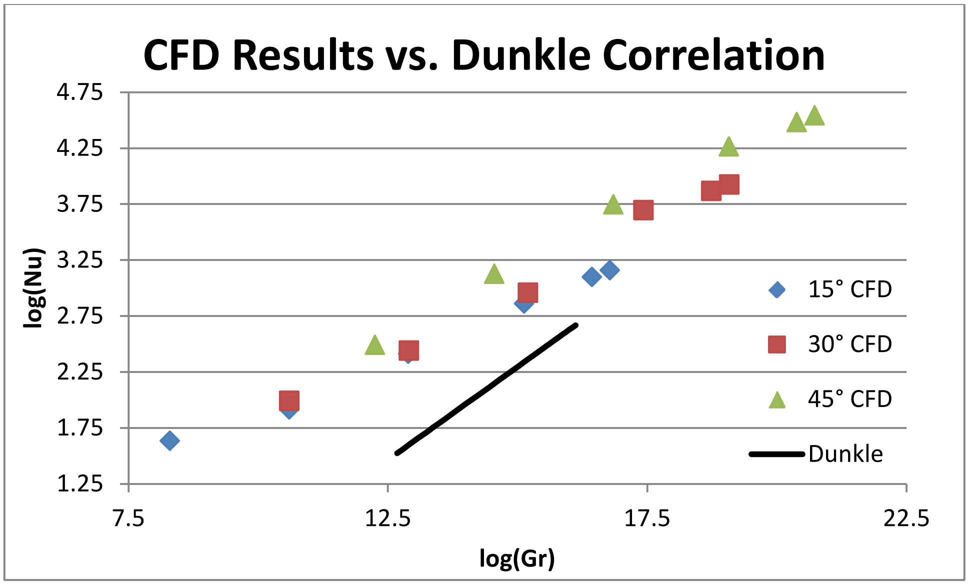

Figure 3-10: Comparison of Dunkle's Correlation with CFD Data

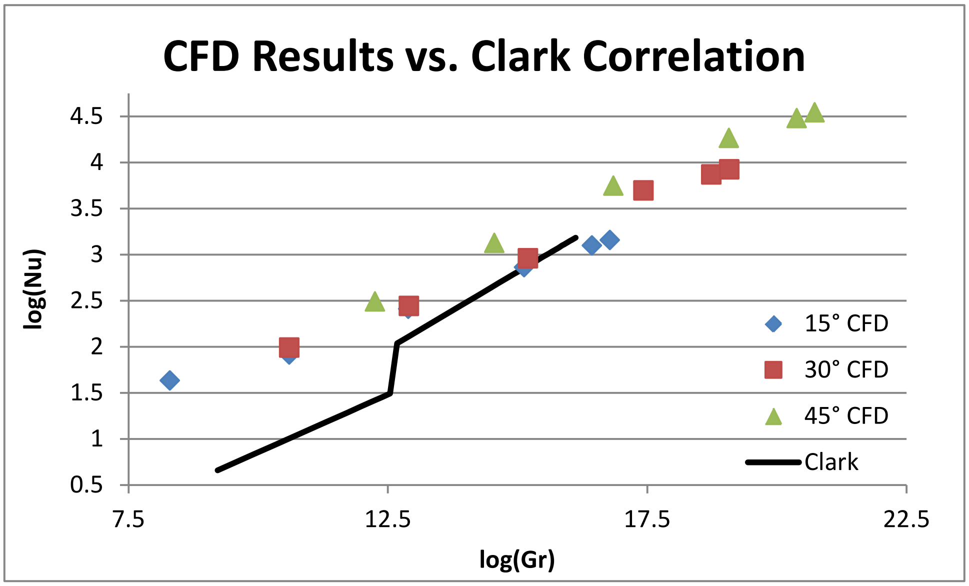

Figure 3-11: Comparison of Clark's Correlation with CFD Data

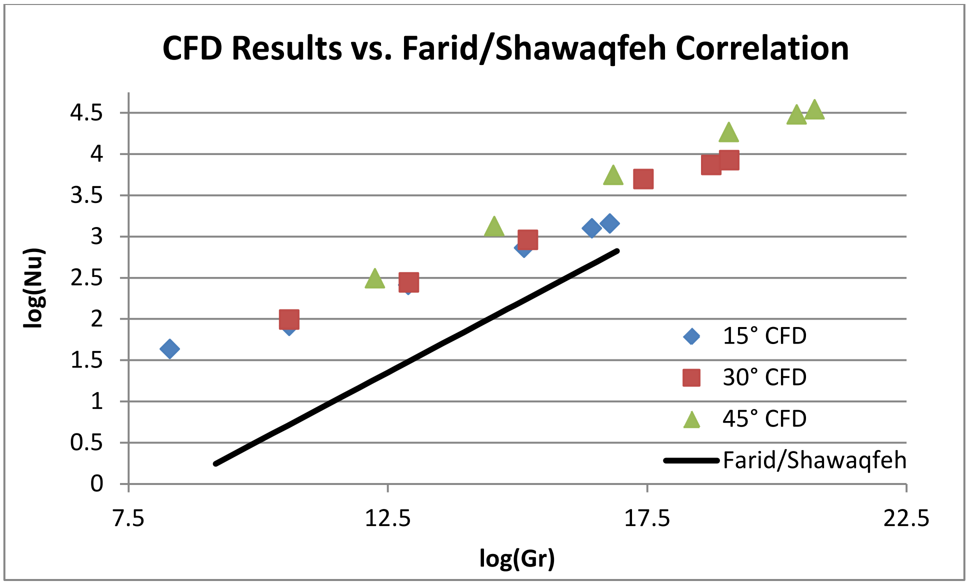

Figure 3-12: Comparison of Farid/Shawaqfeh's Correlation with CFD Data

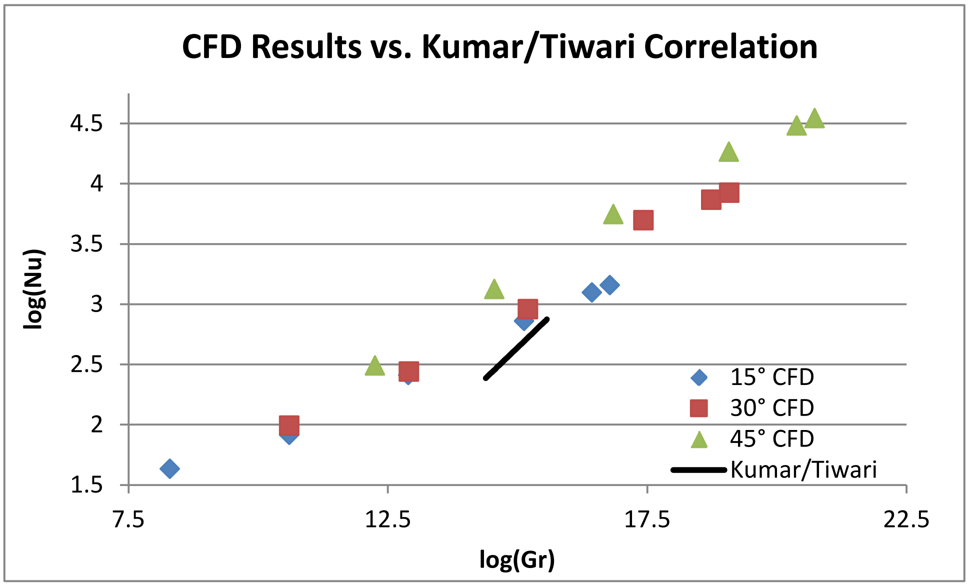

Figure 3-13: Comparison of Kumar/Tiwari's Correlation with CFD Data

3.6 Conclusions

Improving the convection correlations within passive solar stills requires an expansion of the existing correlations to include the specific geometric features of the still. For stills with triangular covers, the current work's correlation is as accurate as Shruti's and can be used over a larger range of Grashof numbers. The correlations presented in this paper can be used for cover geometries with tilt angles ranging from 15^o to 45^o and for Grashof numbers from 4.0×10^3 to 1.0×10^9 (Grashof number range depends on the tilt angle) with less than 37% error.

Further work could be done to refine the meshes in order to further decrease the error caused by the coarse grids used. Also, the range of angles could be expanded to include lower and higher angles. An increase in access to computing resources might even make it possible to model three dimensional effects and improve the correlations even further. In any case, Shruti's correlation is sufficient for most single slope passive stills and can be appropriately modified to estimate the convection of varied cover angles. The current model can be used with acceptable levels of uncertainty and over a wider range of Grashof numbers.

4 RESEARCH CONCLUSIONS

The analyses done previously give some insights to improving solar still performance. Both the radiation analysis and the CFD simulations can be used to improve modeling and optimization of solar still output. General trends seen from both analyses give us a general idea of what direction to take future research and optimization efforts.

4.1 Radiation Model Trends and Conclusions

The radiation model showed that a single slope still can absorb more radiation over the course of the day than any other pentahedron geometry. Assuming this trend holds even after accounting for internal reflections, we can assume that the single slope still is the best design for output per unit basin area. As mentioned in the introduction, maximized insolation will lead to maximized output.

On the other hand, a single slope still may not be the most cost effective, as the cover surface area of the optimized half-pyramid was only 76% that of the optimized single slope. With the half-pyramid absorbing only 3.9% less radiation, this means the half-pyramid might have a cost advantage. If both covers were made of the same material uniformly (that is to say the same material for every cover surface), the half-pyramid would have an economic advantage.

4.2 CFD Convection Modeling

The CFD convection modeling showed one trend that becomes important when modeling a passive solar still. The higher the angle of the cover, the higher the Nusselt numbers tend to be.

As far as comparing the new correlation given here to the existing correlations, it remains difficult to definitively state which one is better than the other. The potential for error with the proposed correlation is high, but the potential for error in the experimental correlations is also high. However, the good agreement between Shruti's correlation and the proposed correlation suggests that both do better than the other correlations when cover geometry needs to be accounted for. This is important when optimizing a solar still, because geometric parameters are generally varied to find the most favorable solution. If more computing resources become available, the error in the CFD correlation could be reduced significantly and the correlation could be extended to include higher and lower angles. In addition, regression could be performed to find a direct relationship between cover angle and the correlation coefficients if enough data is gathered. Such improvements would bring experimental data closer to analytical estimates, and ultimately improve the thermal modeling capabilities of the solar still community.

REFERENCES

[1] National Academy of Engineering. (June 14, 2010). "Provide Access to Clean Water." *Grand Challenges for Engineering*. Web.

[2] United Nations Development Programme. (2006). Human Development Report 2006: Beyond Scarcity: Power, Poverty and the Global Water Crisis. New York: Palgrave Macmillan. Print.

[3] U.S. Environmental Protection Agency. (Nov. 2, 2009). "Gulf of Mexico Program." US EPA. Web.

[4] Tiwari, G.N. and Tiwari, A.K. (2008). *Solar Distillation Practice for Water Desalination Systems.* Kent: Anshan Limited. 37, 43-51, 160, 168, 182-202. Print.

[5] Singh, H.N., Tiwari, G.N. (2004). "Monthly Performance of Passive and Active Solar Stills for Different Indian Climatic Conditions." *Desalination,* 168: 145-150. Web.

[6] Ulgen, Koray. (2006). "Optimum Tilt Angle for Solar Collectors." *Energy Sources,* Part A, 28: 1171–1180. Web.

[7] Tiwari, G.N., Singh, A.K., Sharma, P.B., Khan, Emran. (1995). "Optimization of Orientation for Higher Yield of Solar Still for a Given Location." *Energy Conversion Management,* 36(3): 175-187. Print.

[8] Al-thani, F.N., Nasser, S.H., and Sayigh, A.A. (2000). *World Renewable Energy Congress VI*, 2170-2173. Web.

[9] Al-thani, F.N., Nasser, S.H., and Sayigh, A.A. (2000). *World Renewable Energy Congress VI*, 2174-2177. Web.

[10] Fath, H.E.S., El-Samanoudy, M., Fahmy, K., and Hassabou, A. (2003). "Thermal-economic Analysis and Comparison Between Pyramid-shaped and Single-slope Solar Still Configurations." *Desalination,* 159: 69-79. Web. (accessed 24 April 2012).

[11] Watercone. (2008). "The Product." *MAGE Water Management*. Web.

[12] Ismail, Basel I. (2009). "Design and Performance of a Transportable Hemispherical Solar Still." *Renewable Energy.* 34: 145-150. Web. (accessed 24 April 2012).

[13] Minasian, A.N. and Al-Karaghouli, A.A. (1992). “Floating Vertical Solar Still for Desalination of Marsh Water.” *Renewable Energy.* 2(6): 631-635. Print.

[14] Tiwari, G.N., Mukherjee, K., Ashok, K.R., and Yadav, Y.P. (1986). “Comparison of Various Designs of Solar Stills.” *Desalination.* 60: 191-202. Print.

[15] Ahmed, S.T. (1988). “Study of Single Effect Solar Still with an Internal Condenser.” *International Journal of Solar and Wind Technology.* 5(6): 637.

[16] Madani, A.A. and Zaki, G.M. (1989). “Performance of Solar Still with Intermittent Flow of Waste Hot Water in the Basin.” *Desalination.* 73: 167.

[17] Singh, H.N. and Tiwari, G.N. (2004). “Monthly Performance of Passive and Active Solar Stills for Different Indian Climatic Conditions.” *Desalination.* 168: 145.

[18] Avvannavar, Santosh M., Mani, Monto and Kumar, Nanda. (2008). “An Integrated Assessment of the Suitability of Domestic Solar Still as a Viable Safe Water Technology for India.” *Environmental Engineering and Management Journal.* 7(6): 676. Web. (accessed 26 April 2012).

[19] Taamneh, Yazan and Taamneh, Madhar M. (2012). “Performance of Pyramid-shaped Solar Still: Experimental Study.” *Desalination.* 291: 65-68. Web. (accessed 26 April 2012).

[20] Badran, Ali A., Al-Hallaq, Ahmad A., Salman, Imad A. Eyal, and Odat, Mohammad Z. (2005). “A Solar Still Augmented with a Flat-plate Collector.” *Desalination.* 172: 227-234. Web. (accessed 26 April 2012).

[21] Duffie, John A. and Beckman, William A. (1980). *Solar Engineering of Thermal Processes*, New York: John Wiley & Sons, 216-226. Print.

[22] Siegel, Robert, Howell, John R. and Menguç, M. Pinar. (2010). *Thermal Radiation Heat Transfer*. Boca Raton, Florida: CRC Press I LLC, 819-820. Print.

[23] Dunkle, R.V. (1961). “Solar Water Distilllation: The Roof Type Still and a Multiple Effect Diffusion Still.” *International Developments in Heat Transfer, A.S.M.E., Proceedings of International Heat Transfer,* Part V, 895. (content as cited in Tiwari.)

[24] Clark, J.A. (1990). “The Steady-state Performance of a Solar Still.” *Journal of Solar Energy.* 44(1): 43. (content as cited in Tiwari.)

[25] Shawaqfeh, A.T. and Farid, M.M. (1995). “New Development in the Theory of Heat and Mass Transfer in Solar Stills.” *Solar Energy*. 55: 527.

[26] Shruti, A. and Tiwari, G.N. (1998). “Convective Mass Transfer in Double Condensing Chamber and Conventional Solar Still.” *Desalination.* 115: 181.

[27] Shruti, A. (1999). “Computer Based Thermal Modeling of an Advanced Solar Distillation System: An Experimental Study.” *Diss. IIT Delhi, New Delhi*. (content as cited in Tiwari.)